NAVAL POSTGRADUATE SCHOOL

MONTEREY, CALIFORNIA

THESIS

AN ANALYSIS OF METEOROLOGICAL MEASUREMENTS USING A MINIATURE QUAD-ROTOR UNMANNED AERIAL SYSTEM

by

Christopher R. Machado

June 2015

Thesis Co-Advisors: Peter S. Guest
                                           Andreas K. Goroch

Approved for public release; distribution is unlimited

THIS PAGE INTENTIONALLY LEFT BLANK

1. AGENCY USE ONLY *(Leave blank)*	**2. REPORT DATE** June 2015	**3. REPORT TYPE AND DATES COVERED** Master's Thesis	
4. TITLE AND SUBTITLE AN ANALYSIS OF METEOROLOGICAL MEASUREMENTS USING A MINIATURE QUAD-ROTOR UNMANNED AERIAL SYSTEM		**5. FUNDING NUMBERS**	
6. AUTHOR(S) Christopher R. Machado			
7. PERFORMING ORGANIZATION NAME(S) AND ADDRESS(ES) Naval Postgraduate School Monterey, CA 93943–5000		**8. PERFORMING ORGANIZATION REPORT NUMBER**	
9. SPONSORING /MONITORING AGENCY NAME(S) AND ADDRESS(ES) N/A		**10. SPONSORING/MONITORING AGENCY REPORT NUMBER**	
11. SUPPLEMENTARY NOTES The views expressed in this thesis are those of the author and do not reflect the official policy or position of the Department of Defense or the U.S. Government. IRB Protocol number ____N/A____.			
12a. DISTRIBUTION / AVAILABILITY STATEMENT Approved for public release; distribution is unlimited		**12b. DISTRIBUTION CODE**	

13. ABSTRACT (maximum 200 words)

Naval operational weather products, especially EM prediction, often fail to capture key meteorological features in the boundary layer due to the absence of high-resolution profile data. Quad-rotor sUAS with meteorological sensing capabilities may provide a solution for acquiring vertical profile data at sea. With the use of an RS92 radiosonde, InstantEye small Unmanned Aerial System (sUAS), and a calibrated sensing tower we analyzed the effects a quad-rotor had on the accuracy of temperature and pressure profiles in the surface layer.

In unstable atmospheres temperature measurements made in the surface layer are as accurate as the manufacturers claimed accuracy. In stable atmospheres mixing occurs below 1.3 m, and above 2 m sampled air comes from as much as 2 m aloft. The InstantEye's rotors contribute to the variation in temperature measurement, and this effect is strongest near the surface. The variations introduced by the prop-wash helped suppress natural variations from turbulent fluctuations, but are still present above the surface layer. The InstantEye also introduces a 0.12 hPa pressure bias while in flight due to rotor-induced lift.

14. SUBJECT TERMS Quad-rotor, Surface Layer, Error Analysis, Atmospheric Temperature Profile, UAS, sUAS			**15. NUMBER OF PAGES** 97
			16. PRICE CODE
17. SECURITY CLASSIFICATION OF REPORT Unclassified	**18. SECURITY CLASSIFICATION OF THIS PAGE** Unclassified	**19. SECURITY CLASSIFICATION OF ABSTRACT** Unclassified	**20. LIMITATION OF ABSTRACT** UU

i

THIS PAGE INTENTIONALLY LEFT BLANK

Approved for public release; distribution is unlimited

**AN ANALYSIS OF METEOROLOGICAL MEASUREMENTS USING A
MINIATURE QUAD-ROTOR UNMANNED AERIAL SYSTEM**

Christopher R. Machado
Lieutenant, United States Navy
B.S., University of Maryland, College Park, 2009
MEM, Old Dominion University, 2014

Submitted in partial fulfillment of the
requirements for the degree of

**MASTER OF SCIENCE IN METEOROLOGY AND PHYSICAL
OCEANOGRAPHY**

from the

**NAVAL POSTGRADUATE SCHOOL
June 2015**

Author: Christopher R. Machado

Approved by: Peter S. Guest
                 Co-Advisor

                 Andreas K. Goroch
                 Co-Advisor

                 Wendell Nuss
                 Chair, Department of Meteorology

THIS PAGE INTENTIONALLY LEFT BLANK

ABSTRACT

Naval operational weather products, especially EM prediction, often fail to capture key meteorological features in the boundary layer due to the absence of high-resolution profile data. Quad-rotor small unmanned aerial systems (sUAS) with meteorological sensing capabilities may provide a solution for acquiring vertical profile data at sea. With the use of an RS92 radiosonde, InstantEye sUAS, and a calibrated sensing tower, we analyzed the effects a quad-rotor had on the accuracy of temperature and pressure profiles in the surface layer.

In unstable atmospheres, temperature measurements made in the surface layer are as accurate as the manufacturer's claimed accuracy. In stable atmospheres, mixing occurs below 1.3 m, while above 2 m, sampled air comes from as much as 2 m aloft. The InstantEye's rotors contribute to the variation in temperature measurement, and this effect is strongest near the surface. The variations introduced by the prop-wash helped suppress natural variations from turbulent fluctuations, but are still present above the surface layer. The InstantEye also introduces a 0.12 hPa pressure bias while in flight due to rotor-induced lift.

THIS PAGE INTENTIONALLY LEFT BLANK

TABLE OF CONTENTS

LIST OF FIGURES

LIST OF TABLES

THIS PAGE INTENTIONALLY LEFT BLANK

LIST OF ACRONYMS AND ABBREVIATIONS

A2/AD	Anti-access Area Denial
ABL	Atmospheric Boundary Layer
AG	Aerographer's Mate
AoA	Angle of Attack
AREPS	Advanced Refractive Effects Prediction System
COAMPS	Coupled Ocean/Atmosphere Mesoscale Prediction System
DOD	U.S. Department of Defense
DON	U.S. Department of the Navy
EM	Electromagnetic
GPS	Global Positioning System
ISR	Intelligence, Surveillance, and Reconnaissance
JIFX	Joint Interagency Field Experiment
M	Modified Index of Refractivity
MRMUA	Multi-rotor Miniature Unmanned Aircraft
NOAA	National Oceanic and Atmospheric Administration
PSI	Physical Sciences Inc.
RH	Relative Humidity
RPA	Remotely Piloted Aircraft
RTD	Resistance Temperature Detector
sUAS	Small Unmanned Aircraft System(s)
TC	Thermocouple
UAS	Unmanned Aerial System(s)
UAV	Unmanned Aerial Vehicle

THIS PAGE INTENTIONALLY LEFT BLANK

ACKNOWLEDGMENTS

THIS PAGE INTENTIONALLY LEFT BLANK

I. INTRODUCTION

A. UNMANNED AERIAL SYSTEMS

The use of unmanned aircraft in military applications is nothing new. Remotely piloted airplanes can be traced back to as early as World War I in which British researcher A. M. Low developed his "Aerial Target" to fly ordinance-laden planes into enemy positions and aircraft (Taylor 1977). While the concept appealed to military leaders, the technology was severely lacking to provide any decisive advantage on the battlefield. Years later, in World War II, more robust aircraft with superior control systems saw action in combat, but still failed to demonstrate their necessity as part of a military arsenal (Keane and Carr 2013).

Despite these early failures, interest in unmanned aircraft persisted in military circles throughout the years. Today advances in communications, signal processing, and manufacturing techniques have enabled aircraft designers to provide militaries with effective mission-capable remotely-piloted assets. Common names for these include drones, unmanned aerial vehicles (UAV), remotely piloted aircraft (RPA), unmanned aerial system (UAS), or small UAS (sUAS). A UAS is defined as, "a system whose components include the necessary equipment, network, and personnel to control an unmanned aircraft" (JCS 2010). For the purposes of this document, we will use only the term UAS and sUAS to describe unmanned aircraft, as the definition provides a broader perspective for describing all components related to unmanned flight.

Today the U.S. military maintains the largest investment in UAS technology compared to any other organization. As of July 1, 2013, the DOD maintained nearly 11,000 UAS in its inventory, allocating $3.8 billion from the FY2014 budget. Despite projected budgetary cutbacks, funding is expected to grow by 17% through FY2018 (Pentagon 2014). Such commitment to UAS integration demonstrates the utility UAS provide on the battlefield. The platforms in use today perform a variety of missions including intelligence, surveillance,

and reconnaissance (ISR), as well as combat strike missions. The focus of future UAS military technology will be primarily centered on ensuring dominance in contested airspace, and superiority in anti-access area denial (A2/AD) scenarios. This not only requires improvements to communication and sensing networks for tactical efficiency, but also necessitates an improvement in environmental awareness to better assess risk and exploit certain weather phenomena such as electromagnetic (EM) propagation features.

B.   WEATHER AND EM PROPAGATION PREDICTION

Understanding the weather is a critical component in combat effectiveness. Every military asset can be adversely affected by unfavorable weather conditions; therefore, operational commanders depend on accurate forecasts. This is particularly challenging for the Navy where operations take place over open water and routine meteorological measurements are sparse. In the past, naval forecasters, referred to as Aerographer's Mates (AGs), utilized weather balloons to sample the vertical structure of the atmosphere. This not only assisted in developing forecasts for daily operations, but also improved shore-based computer weather prediction models since the data could easily be forwarded and integrated into the model. Unfortunately, the Navy's operational weather balloon program was terminated in 2011 (OPNAV N2/N6F5 2010), causing tremendous uncertainty in vertical structure of the atmosphere in crucial regions. Since then AGs have had to rely exclusively on model data, satellite images, and surface observations to perform their duties while at sea.

A consequence of the knowledge gap in vertical atmospheric structure is the inability to create accurate EM predictions products. These products predict how various communication and radar systems will perform based on given atmospheric conditions. The atmosphere, particularly near the surface, can experience large diurnal and daily changes. These variations influence the effective range over which a radar system can detect a target. An aircraft might have an extended communication range one day, and a severely limited range

the next. EM signals also have the potential of being intercepted or jammed, so understanding the performance parameters of systems belonging to both friendly and adversarial forces is crucial in wartime. Recognizing the importance of EM propagation in future warfare, the Chief of Naval Operations ADM Jonathan Greenert stated in 2011, "Control of information, much of it through the electromagnetic spectrum, is already growing more important than the control of territory in modern warfare" (OPNAV N2/N6 2012). EM waves are the means with which information is exchanged on the battlefield, and knowledge of how they propagate can mean the difference of exploiting an adversary's activities, or being exploited by them.

EM signals in radio frequencies are influenced by three atmospheric properties: temperature, pressure, and relative humidity (Ko et al. 1983). Variations of these parameters are used by the military's Advanced Refractive Effects Prediction System (AREPS) to analyze how various radar and communication systems are expected to operate (SPAWAR 2006). While AREPS has the capability for the user to manually input atmospheric parameters (e.g., from a weather balloon), the atmospheric variables are now usually obtained through the Coupled Ocean/Atmosphere Mesoscale Prediction System (COAMPS™) weather model. However, poor vertical resolution in COAMPS™ output presents a major disadvantage. Many assumptions about the vertical profile are made, which can have a dramatic effect on EM propagation products. In the atmospheric boundary layer (ABL), or the layer approximately 100 to 3000 meters above ground (Stull, 1998), surface fluxes can dramatically affect temperature and humidity profiles, often missed by COAMPS™. Consequently, AREPS may fail to accurately capture significant propagation features.

C. WEATHER SENSING WITH UAS

With the increasing use of military UAS, it seems logical to employ these aircraft to sample the atmosphere. Since most UAS are smaller and lighter than traditional aircraft due to lack of a human pilot and the accompanying safety

systems, they tend to be more vulnerable to adverse weather conditions such as wind gusts and icing. Atmospheric sensors installed onboard could not only serve to alert operators of dangerous conditions, but the data could also be collected for weather model inputs to improve future forecasts.

Some UAS, such as the NOAA-owned Global Hawk, are used exclusively for high altitude atmospheric measurements (Braun 2013). These aircraft have been outfitted with an array of meteorological sensors used to conduct research in tropical cyclones. The DOD is also mounting meteorological sensors, and several noteworthy experiments have occurred in recent years. BAE Systems' Manta and Boeing's Scan Eagle were tested in 2011 and 2012, demonstrating the first known UAS measurements of heat, water vapor and momentum fluxes at low altitudes (Reineman 2013). In another experiment as part of exercise Trident Warrior 2013 (TW13), the Scan Eagle was again tested to capture boundary layer profiles, and successfully demonstrated that atmospheric measurements collected by UAS could be ingested into COAMPS improving short-range forecasts (NRL 2015). While this may at first seem promising, TW13 also revealed that due to Scan Eagle's safety requirements restricting low-level flight, significant EM propagation features were not captured when compared to a tethered sensor in the lowest 100 meters.

UAS such as the Manta or Scan Eagle are fairly large enough fixed-wing aircraft to require sophisticated launch and recovery apparatuses and a team of skilled workers to operate and maintain them. Their procurement cost is also substantial, thus explaining any apprehension toward near-surface flight. A commander in possession of one or more UAS must also balance a set of demanding mission requirements with all available resources. For these reasons, a fixed-wing UAS already in service is not an ideal candidate to be used as a dedicated meteorological sensor. sUAS, on the other hand, may be well suited to serve in this capacity, and may be a feasible alternative to their larger and more expensive counterparts.

Small quad-rotor helicopters, also known as quad-copters, are a class of sUAS. Quad-rotor sUAS, as their name implies, have four rotors to generate lift, making them very stable aircraft. They can also be very compact, measuring less than one-half meter in width and weighing only a couple kilograms. Unlike their larger fixed-wing counterparts, a single person with very limited training can operate quad-rotor sUAS. Due to large-scale commercialization of quad-rotors over the past decade, their costs have significantly declined to only hundreds or a couple thousand dollars; a mere fraction of the cost associated with traditional DOD UAS. The simplicity and affordability of quad-rotor sUAS make it feasible to employ them on a large scale as dedicated meteorological sensing devices. A vast network of worldwide sensors in the ABL could significantly improve model products and operational EM propagation forecasting techniques.

D.   RESEARCH OBJECTIVES

The use of small quad-rotor sUAS for meteorological sampling is a fairly novel concept with very little literature existing on the subject. The aim of this document is to investigate how the performance of meteorological sensors attached to a miniature quad-rotor sUAS is affected while in flight. Specifically, temperature and pressure datasets were collected during Joint Interagency Field Exercises (JIFX) in 2014 for both stable and unstable atmospheres. Our analysis is an investigation of sensing performance under these two conditions.

THIS PAGE INTENTIONALLY LEFT BLANK

II. BACKGROUND AND CONSIDERATIONS

The aerodynamics and various motions of air surrounding an aircraft with a spinning rotor are complex. Four rotors operating in an equilateral array add another layer of complexity to the problem. Furthermore, atmospheric conditions in the boundary layer are also turbulent and difficult to quantify from single point measurements. Interaction between air and the earth's surface drive many processes in fluid motions and gradient distributions. To understand how a quad-rotor sUAS in flight affects the ABL meteorological conditions that it is supposed to measure, it is important to first develop some background information pertaining to these two subjects.

A. QUAD-ROTOR MECHANICS

The principles governing quad-rotor performance are related to the helicopter. The following discussion on rotor flight performance is largely based on the work of Leishman (2006).

1. Momentum Theory

A general helicopter undergoes many different flight configurations such as hovering, forward motion, and climb and descent. The mass flow through the rotor is a complicated process of varying velocities accompanied by a sequence of pressure-induced vortices in the slipstream (or wake) that differ between each configuration of flight. However, rotor performance can be analyzed through a simplified method in which assumptions are made about the model. This method is well adopted in the field of aerodynamics known as the Rankine-Froude momentum theory.

The model assumes that the air is incompressible and inviscid, which generates no shear within the fluid. The flow through the rotor is one-dimensional, steady and uniform, and does not impart a rotational component to the traversing fluid. While these assumptions will inevitably introduce errors into

7

the results, the simplification outweighs these errors, which can be mitigated through an appropriate correction factor applied to the final result (Layton 1984). Momentum theory also assumes that the rotor is an infinitesimally thin actuator disk, which supports the thrust generated by the rotational motion of the blades. Work is done on the rotor from torque applied by the rotor shaft, which is converted into a net gain of kinetic energy within the rotor wake.

a.   Stationary Flight

A hovering helicopter is the most basic configuration to analyze performance. There is zero vertical or horizontal velocity, and the rotor flow field is said to be azimuthally axisymmetric. Consider a finite control volume S containing the rotor and surrounding air volume as shown in Figure 1. The top plane is at a distance far above the rotor and the fluid is quiescent (i.e., $V_C = 0$). Plane 1 and plane 2 represent the area just above and below the rotor, respectively. Given an infinitesimally thin rotor plane, the fluid velocity is equal through these two planes at $V_C + v_i$; however, a pressure differential exists across the rotor plane enabling the thrust needed to counter the weight of the aircraft. Far below the rotor plane is the wake plane, denoted as ∞, with the wake velocity $V_C + w$. From the unit normal area vector, denoted by $d\vec{S}$, and the conservation of mass we can express the mass flux through the control volume as

$$\iint_S \rho\, d\vec{V} \cdot d\vec{S} = 0, \tag{1}$$

where ρ is air density.

Put another way, the mass flowing into the control volume is equal to the mass flowing out. The mass flow rate $\dot{m}$ must also be consistent through any portion of the control volume. Hence,

$$\dot{m} = \iint_\infty \rho \vec{V} \cdot d\vec{S} = \iint_1 \rho \vec{V} \cdot d\vec{S} = \iint_2 \rho \vec{V} \cdot d\vec{S}, \tag{2}$$

8

which is further reduced by the one-dimensional incompressible flow assumption

$$\dot{m} = \rho A_\infty w = \rho A v_i .$$ (3)
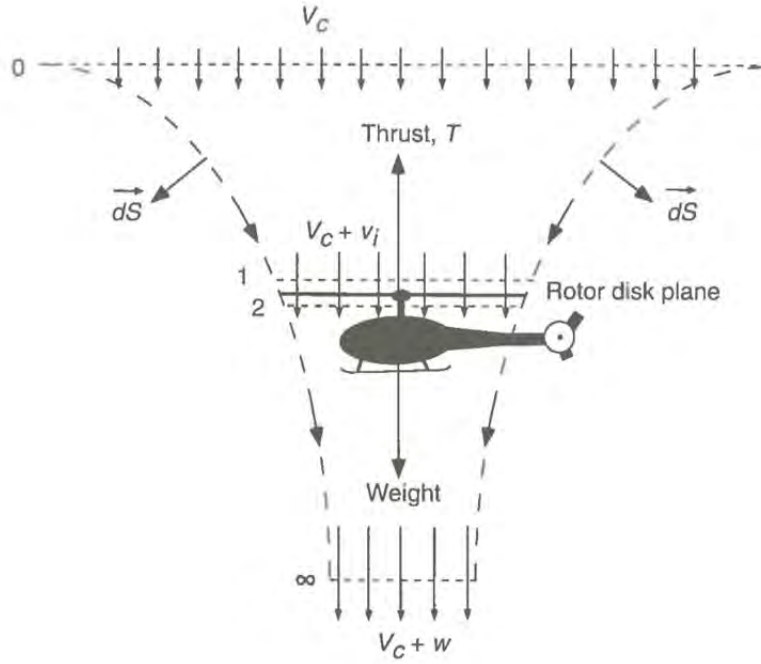
Figure 1.   Flow model for momentum theory analysis of a rotor in hovering flight (from Leishman 2006).

The work done on the rotor is equal to the kinetic energy imparted into the slipstream per unit time, also known as power Tv_i, where T is the upward force or thrust exerted by the rotor. Power can then be expressed as

$$Tv_i = \iint_\infty \frac{1}{2}\rho(\vec{V}\cdot d\vec{S})\vec{V}^2 - \iint_0 \frac{1}{2}\rho(\vec{V}\cdot d\vec{S})\vec{V}^2 .$$ (4)

However, the velocity at plane 0 is nominally zero, eliminating the right hand term. Thus the equation reduces to

$$Tv_i = \frac{1}{2}\dot{m}w^2$$ (5)

$$v_i = \frac{1}{2}w. \tag{6}$$

Combining Equations (3) and (6) provides the relationship

$$\rho A v_i = \rho A_\infty w = \rho A_\infty \left(2v_i\right). \tag{7}$$

Stated another way, the wake velocity area is half the area of the rotor disk.

From the velocity-area relationship, fluid motion about a rotor plane can be approximately depicted. However, with three additional rotors on a quad-rotor sUAS the flow becomes a bit more complicated. Applying the assumptions of momentum theory to a quad-rotor during hovering flight, a graphical representation of fluid flow can be constructed as shown in Figure 2. Given a wake velocity of approximately 4 m/s, and four rotors placed in a square pattern each with a radius of 7.5 cm, the control volume is now unique. There is a single quiescent plane at $V = 0$ diverging into four separate slipstreams as it passes through the rotor plane as depicted by the green square plane of Figure 2. To minimize slipstream influence on an attached meteorological sensor, ideal placement would be somewhere below the rotor plane and outside of the slipstreams.
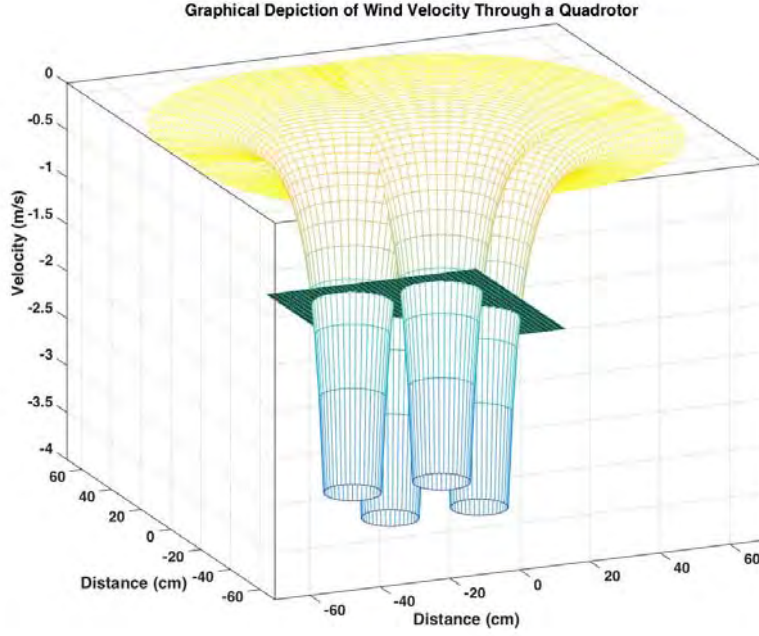
Figure 2.   Graphical depiction of fluid velocity through a quad-rotor sUAS

b.   *Climb and Descent*

While hovering flight is relatively straightforward to analyze, more complex configurations need to be considered for a more comprehensive understanding of fluid flow through a rotor. Climbing and descending are necessary maneuvers for any aircraft, especially one designed to profile the lower atmosphere. When a rotor experiences vertical motion, the air far above and below can also be seen as moving vertically as experienced from the rotor's point of view. This addition of velocity changes the various forces involved in flight.

In a climbing configuration $V_C > 0$, and there is a net upward force. The mass flow rate can be rewritten as

$$\dot{m} = \rho A_\infty (V_C + w) = \rho A (V_C + v_i) \tag{8}$$

Likewise, the thrust produced is now

$$T = \dot{m}(V_C + w) - \dot{m}V_C = \dot{m}w \tag{9}$$

11

$$T = \rho A(V_C + v_i)w = 2\rho A(V_C + v_i)v_i. \tag{10}$$

Now let v_h^2 equal one-half the thrust over density and area,

$$\frac{T}{2\rho A} = v_h^2 = v_i^2 + V_C v_i. \tag{11}$$

Rewriting (11) as a quadratic, it has the solution

$$0 = \left(\frac{v_i}{v_h}\right)^2 + \frac{V_C}{v_h}\left(\frac{v_i}{v_h}\right) - 1 \tag{12}$$

$$\frac{v_i}{v_h} = -\left(\frac{V_C}{2v_h}\right) \pm \sqrt{\left(\frac{V_C}{2v_h}\right)^2 + 1}. \tag{13}$$

From our flow model, v_i / v_h must always be positive for climbing flight, eliminating the negative solution. The increase in climb velocity implies a decrease in the rotor-induced velocity, which is referred to as the normal working state of the rotor (Figure 3). The limit is reached, however, at hovering flight just before descending. When $-2v_h \leq V_C \leq 0$ the velocity at any plane can be either upward or downward creating a complex and turbulent flow pattern. Momentum theory is no longer applicable in this region. The slipstream will exist entirely above the rotor flowing in reverse direction when $V_C < -2v_h$. The rotor now extracts power from the slipstream and is referred to as the windmill brake state. Since $V_C < 0$ during the descent, Equations (8) through (13) can be reassessed to form the solution

$$\frac{v_i}{v_h} = -\left(\frac{V_C}{2v_h}\right) \pm \sqrt{\left(\frac{V_C}{2v_h}\right)^2 - 1}. \tag{14}$$

Again, there are two solutions, but only the negative version is valid to ensure $v_i / v_h \leq 1$. This is logical since a reduction in induced rotor velocity results in a faster descent. Theoretically, rotor-induced velocity contributions should be

negligible to ensure the accuracy of atmospheric measurements. Favorable conditions exist during periods of climbing and of rapid decent. Slow descent is unfavorable since the assumptions of momentum theory are no longer valid, and the stream velocity is unpredictable, creating turbulent conditions within the fluid.
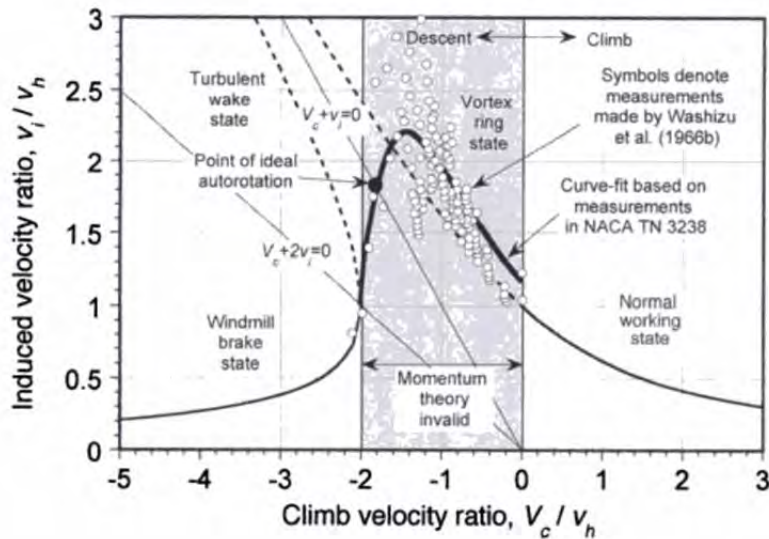
Figure 3. Induced velocity as a function of climb and descent from momentum theory (from Leishman 2006).

c. Horizontal Motion

In the previous sections on helicopter dynamics, we were able to merge momentum theory from a traditional rotorcraft to a quad-rotor model. However, the horizontal motion of a quad-rotor is fundamentally different than a traditional helicopter system. Traditional helicopters only have two rotors and are used in one of two ways, (1) both rotors are used to generate thrust, but rotate in opposite directions to counter the rotor-induced torque, or (2) one rotor is used to generate thrust, and a smaller rotor is used to counter the torque acting on the fuselage. Horizontal motion is accomplished by changing the angle of attack (AoA) of the rotor plane and controlled through the adjustment of the rotor blade pitch and angle relative to the drive shaft.

13

By contrast, miniature quad-rotor sUAS have rigid rotor blades that do no vary in pitch and angle. The four rotors are equally separated in a square pattern, and each spins in the opposite direction as the rotor adjacent to it, balancing the four torque forces (Figure 4). There are only four control inputs (i.e., the rotation speed of each rotor) to regulate the aircraft's pitch, roll and yaw.
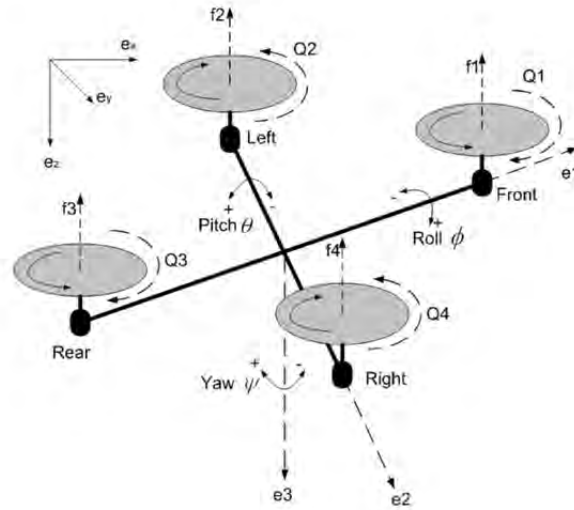
Figure 4.   Forces acting on a quad-rotor aircraft
(from Tayebi and McGilvray 2006).

Horizontal movement is achieved by changing the pitch or roll of the airframe by changing the speed of one or more rotors. The thrust generated by the four rotors is no longer perpendicular to the ground since the rotor plane is tilted at an angle. As a consequence, the flow through the rotors is no longer axisymmetric since the thrust generated is partially transferred to into a horizontal component for movement. The streamline in this configuration is also non-perpendicular to the ground and is angled in the opposite direction of movement. The angle of the streamline could affect atmospheric measurements if the sensor should find its way into the rotor-induced velocity field. Therefore, a meteorological sensor would likely perform best when positioned near the front of the aircraft.

14

2. Vortices

Vortices are a byproduct of lift generated by an airfoil. The pressure differential that exists on either side of the airfoil creates lift. However, at the wing tip the solid boundary disappears, and the difference of pressure must be equalized. The high pressure under the airfoil flows toward the lower pressure above the wing, and the result is a wake vortex. A rotor is an airfoil rotating at high speeds, and as such Leishman explains that a set of vortices are created that follow the rotation of movement. Since the slipstream velocity is downward in a hover or climbing configuration, the vortices will also drift downward creating turbulence in their path (Figure 5).
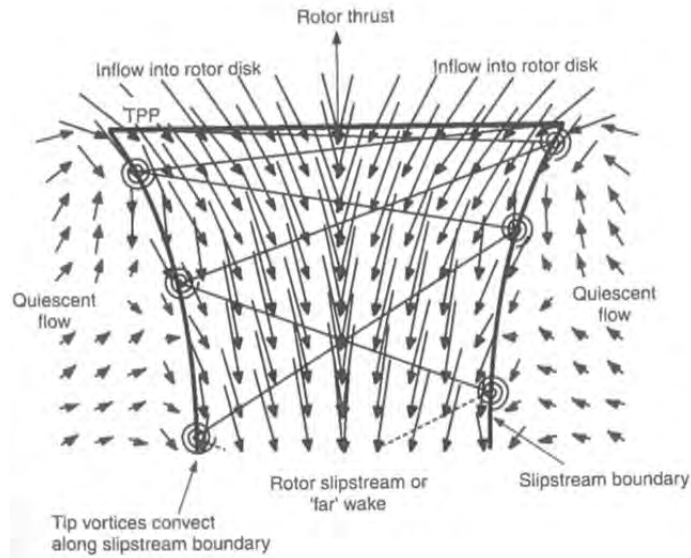
Figure 5.   Velocity field of a two-bladed rotor operating in a hover
(from Leishman 2006)

Turbulence from vortices complicates the flow structure around the aircraft. This is troubling from a meteorological perspective as the rotational energy can promote mixing of the surrounding fluid affecting the accuracy of measurements. This topic is not well understood, and the extent to which mixing affects the environment is in part a goal of this experiment.

3. Ground Effect

Another phenomenon affecting helicopter performance is ground effect. This occurs when the aircraft operates at very low altitudes, and the earth's surface constrains the development of its rotor wake. This has several implications for low-level flight, but predominantly affects the power-to-thrust ratio. When ground effect is present, less power is needed to achieve the necessary thrust required to sustain flight (Leishman 2006). Shown in Figure 6, the ground is a boundary to the streamline flow in the presence of ground effect. As a result, the slipstream rapidly expands as it approaches the ground, altering the slipstream and rotor-induced velocities. From momentum theory, these velocities are related to the power and thrust requirements.
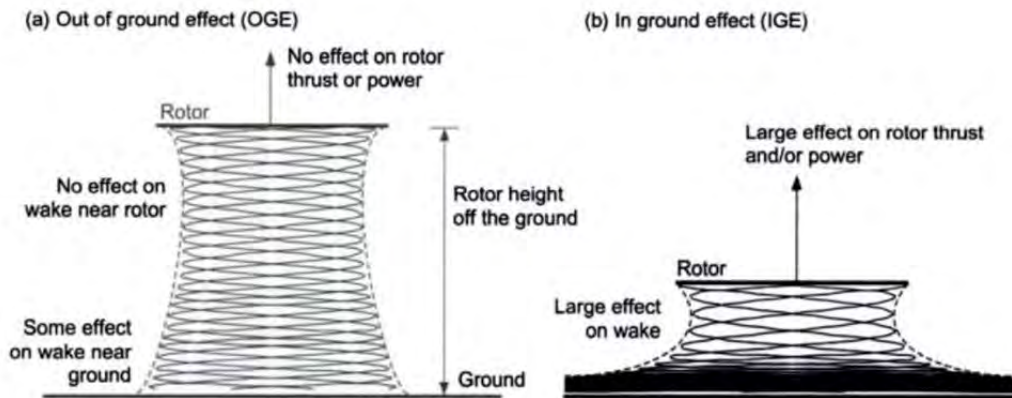
Figure 6.   Wake behavior: (a) Out of ground effect, (b) In ground effect
(from Leishman 2006)

Ground effect's influence on rotor performance varies by altitude. A rotor closer to the ground will experience more slipstream restriction and have a higher thrust-to-power ratio than a rotor at a higher altitude. According to Leishman (2006), empirical observations suggest that significant performance effects due to ground effect occur below an altitude of one rotor diameter. To sufficiently minimize ground effect, an altitude of at least two rotor diameters is recommended.

B.   SURFACE LAYER METEOROLOGY

The atmosphere is composed of several horizontal layers. The region where weather occurs is the troposphere, which extends from the surface to an average altitude of 11 km. In the lowest portion of the troposphere is the boundary layer, defined by Stull (1988) as, "That part of the troposphere that is influenced by the presence of the earth's surface, and responds to surface forcings with a timescale of about an hour or less." The boundary layer's tendency to change rapidly has significant impacts to low-level meteorology. The ground absorbs much of the incoming solar radiation, and in turn the warming ground heats the atmosphere above it through turbulent fluxes and emitting radiation. The energy transfer between the earth's surface and lower atmosphere is distributed through a process called turbulent transport in which warm eddies develop near the ground and are lifted aloft by their buoyancy.

The lowest part of the boundary layer is called the surface layer. Stull (1988) refers to this layer as, "The region at the bottom of the boundary layer where turbulent fluxes and stress vary by less than 10%, decreasing above that in the ABL." In other words, the energy transfer is strongest very close to the surface. The surface layer is important to understand since the majority of the data collected in the experiment was sampled in this region.

1.   Potential Temperature

Potential temperature (θ) is a conserved variable in an adiabatic process, accounting for changes in pressure (Petty 2008). When comparing a sample of vertical temperatures it is important to use potential temperature since according to the ideal gas law temperature and pressure are interdependent. The temperature can be corrected for the pressure change by considering potential temperature defined as

$$\theta = T \left(\frac{P_o}{P} \right)^{0.286} ,$$ (15)

where T is temperature in degrees Kelvin, P is the air pressure in hPa, and P_o is a reference pressure normally 1000 hPa. However, boundary layer work requires using the surface pressure so (15) can be approximated by

$$\theta = T + \left(\frac{g}{C_p} \right) z,$$ (16)

where z is the height in meters above the ground, and (g/C_p) is the dry adiabatic lapse rate of 0.0098 K/m, composed of g, the acceleration due to gravity, and C_p, heat capacity at constant pressure (Stull 1988).

2. Humidity

Humidity is an important quantity affecting EM propagation through the atmosphere. The amount of moisture a parcel of air can hold is directly proportional to that parcel's temperature. Saturation will occur if the moisture content of a parcel equals its temperature limit. Often relative humidity (RH) is used to describe this relationship as a percentage, and is calculated

$$RH = \frac{e}{e_s(T)} \bullet 100,$$ (17)

where e is the actual vapor pressure, and $e_s(T)$ is the saturation vapor pressure. Relative humidity is commonly measured and reported by weather sensors. However, when comparing a set of vertical measurements in the presence of a temperature gradient, specific humidity (q, the ratio of mass of water to the mass of air) is more convenient to use since it is a conserved quantity. Specific humidity is calculated

$$q = \frac{w}{1+w},$$ (18)

where w is the mixing ratio, defined as the ratio between the mass of water vapor to the mass of dry air.

III. EXPERIMENT

A. METHODOLOGY

Testing was performed exclusively at McMillan Airfield, located at Camp Roberts, CA, as part of the Joint Interagency Field Experimentation (JIFX) program in May, August, and November 2014. An InstantEye Mark 2 Gen 3, produced by Physical Sciences Inc. (PSI), was flown in an open field next to a calibrated meteorological observation tower. The tower was in constant operation over the course of each multi-day JIFX measuring and recording pressure, wind, soil parameters, and seven separate levels of temperature and relative humidity. The tower was strategically placed away from obstructions in an open field to minimize localized weather effects.

To measure atmospheric parameters onboard the sUAS, a Vaisala RS92 radiosonde was attached to the underside of the InstantEye. Originally designed as an instrument for weather balloons, the radiosonde proved to be an excellent instrument for this experiment due to its light weight, comprehensive sensing package, and communication system. When in operation, the radiosonde samples temperature, pressure, and relative humidity while transmitting its data in real time to a computer located in a nearby hangar.

Test flights were conducted at various times to collect a diverse data set. Of the flights that were later analyzed, five occurred during daylight hours when the sun's warming effect produced an unstable temperature profile near the observation tower, and two were conducted just before sunrise when the effect of radiative cooling was at its maximum, producing a very stable temperature profile. Security measures in place at Camp Roberts made access to the tower before 6:00 AM difficult, limiting the amount of testing that could be conducted in a stable atmosphere.

Figure 7.   Physical Sciences Inc. InstantEye with
Vaisala Radiosonde Attached

Figure 8.   Meteorological Observation Tower with
seven sensor levels and one wind level.

A typical test flight involved hovering the aircraft at a level corresponding to one of the seven sensors on the observation tower. While the radiosonde collected atmospheric information in flight, the corresponding tower sensor served as a reference instrument recording temperature and relative humidity unaffected by processes produced by the aircraft. Synchronization between the tower and radiosonde was crucial for proper analysis, and achieved through the use of an audio recorder. Recordings were used to document time offsets between the observation tower and the radiosonde computer, as well as provide exact timing of aircraft vertical position.

B.   INSTANTEYE MK 2 GEN 3

PSI's InstantEye was designed for tactical level ISR operations in urban environments giving small ground units situational awareness through the use of its onboard cameras. This sUAS was chosen for the experiment due to its already existing employment within the DOD, active support from PSI. It is likely that, any quad-rotor sUAS capable of carrying the radiosonde payload could also be used in a similar manner.

The InstantEye measures 25 cm across between rotor axes, with each of its four rotors measuring 20.3 cm diameter, and weighs only 320 g without battery or payload. It is capable of operating in all weather, temperatures ranging from -18 to 49 C, and can endure winds of 13 m/s. The endurance rating is dependent on payload weight, battery charge, and airfoil efficiency, but typical flights during the experiment lasted about 15 to 20 minutes before battery replacement was needed.

Built into the InstantEye are three cameras at different angles, GPS, and pressure sensor, which send information to the operator via the flight controller screen. The camera image is displayed in real time on the controller serving as a tool for navigation when visual contact is lost. The GPS device provides real time location coordinates of the aircraft, and also serves to hold the aircraft's lateral position under autonomous flight making it less susceptible to unwanted

movement due to prevailing and gusting winds. The GPS information is part of the InstantEye's internal circuitry and was not recorded during the experiment. The pressure data measured from the pressure sensor is unavailable to the user, but the information is converted to altitude and displayed in feet. The InstantEye responds to slight changes in pressure to control its climb rate and maintain its altitude. Like the GPS data, the InstantEye pressure measurements were not recorded during the experiment and only used for avionics control.

Figure 9.   PSI InstantEye Front and Bottom View

C.   RADIOSONDE

For the purpose of the experiment, Vaisala's RS92 radiosonde was an ideal meteorological sensing device to be used onboard the aircraft. Vaisala has been a trusted name for reliable and accurate meteorological sensors for decades, and the RS92 is a model is used worldwide for vertical atmospheric sampling attached to weather balloons. According to Vaisala's datasheet, the sensing package includes a single wire capacitance temperature sensor, dual heated thin-filmed capacitance relative humidity sensors, and a micromechanical silicon pressure sensor. Capacitive sensors are not influenced by magnetic variations (Kruis et al. 1998), and this is important since the sUAS is controlled by electric signals, which generate magnetic disturbances very close to the RS92 sensors.

The RS92 also contains a GPS device to track lateral movements aloft used to calculate wind speed and direction while attached to a drifting balloon. Since the sensor was attached to a controlled aircraft designed to resist wind variations, wind data collected from the RS92 during the experiment were irrelevant. It was thought that the GPS coordinates collected might be able to help determine lateral movements of the aircraft during the experiment, but the resolution was too coarse to extract any meaningful information.

Another feature of the RS92 is a fully digital transmission signal on the 400–405 MHz meteorological band. In general, there are two methods of collecting data from a sensor attached to the aircraft, 1) the data is stored on a local memory device, then extracted to a computer once the aircraft is recovered, or 2) the data is streamed wirelessly while in flight to a recording device on the ground. Locally stored data as in option (1) presents some risk. If the aircraft crashes (as it did many times during the experiment), or is unrecoverable, there is the potential of also losing the data collected. For the experiment a locally stored device might be have been adequate since most of the flights took place over land at low levels, but in a real at-sea application altitudes would be much higher over open ocean furthering the risk of non-recoverability. While a

specifically designed sensor meeting all the requirements for mission deployment is preferred, the RS92 is an affordable option and could be used immediately for fleet deployment, making it an ideal test instrument for this experiment.

Figure 10.   Vaisala Radiosonde RS92-SGP

SENSOR	OPERATING RANGE	ACCURACY
Temperature	-90 to 60 C	± 0.5 C
Pressure	3 to 1080 hPa	± 1 hPa
Relative Humidity	0 to 100%	± 5%

Table 1.   Vaisala Radiosonde RS92-SGP specifications
(from www.vaisala.com)

D. OBSERVATION TOWER

The tower was constructed using a metallic tripod extending upward to 6.2m where a Vaisala WXT520 weather station was mounted. For the purpose of the experiment only barometric pressure, wind speed, and wind direction were of any value by the WXT520. Separate temperature and relative humidity probes were installed along the vertical axis of the tripod with approximately logarithmic spacing. The spacing ensured a near linear temperature sampling distribution due to the rapid temperature differential caused by surface heat flux (Table 1).

Tower Level	Height (m)
WXT520	6.20
7	4.93
6	2.44
5	1.30
4	0.66
3	0.34
2	0.19
1	0.11

Table 2.   Observation tower sensor heights

Seven Rotronic MP100H relative humidity sensors with accompanying Pt100 1/10 DIN RTD temperature sensors were encased in PVC piping attached to the tripod. The portion of housing wall enclosing the sensors was double layered, fitted with a shield to minimize contamination from solar heating. An aspirator was used in the bottom six levels ensuring a uniform 3.5 m/s flow over the sensors. The seventh level was a later addition after the tower's original

construction, and because of this, a separate aspirator and ventilation path with an unknown flow rate exist in the highest temperature and relative humidity sensors.

During the experiment an additional temperature probe with a faster response time was required to capture turbulent temperature variations. A Campbell Scientific FW05 fast response thermocouple was installed at level four outside the PVC housing exposed to the elements. According to FW05 brochure, solar contamination is negligible due to the small diameter of the FW05 wire (0.0127 mm), and a radiation shield is not required. Each of the tower sensors were linked to a Campbell Scientific CR3000 Micrologger, which recorded at a sample rate of 10 seconds (0.1 Hz). The accuracy of each instrument is summarized in Table 3.

SENSOR	MFR.	MODEL	OPERATING RANGE	ACCURACY
Pressure	Vaisala	WXT520	600 to 1100 hPa	± 0.5 hPa (0–30 C)
Wind Speed	Vaisala	WXT520	0 to 60 m/s	± 3% (10 m/s)
Wind Direction	Vaisala	WXT520	0 to 360°	± 3°
Temperature (RTD)	Rotronic	Pt100 1/10 DIN	-40 to 60 C	$\pm (0.3 + 0.005*t)$
Temperature (TC)	Campbell Scientific	FW05	-270 to 1000 C	± 1.7 C
Relative Humidity	Rotronic	MP100H	0 to 100%	± 1%

Table 3.   Observation tower sensor specifications

IV.   ERROR ANALYSIS

To determine whether the InstantEye prop-wash or other contamination effects have any influence over the accuracy of the onboard radiosonde sensors, a method must first be developed to determine an acceptable range of accuracy. No matter how carefully an experiment is carried out, every measurement contains within it some degree of error. This chapter is aimed at examining the various sources of errors and uncertainties introduced in the experiment, and to determine an appropriate correction and tolerance for measured values.

A.   RANDOM AND SYSTEMATIC ERRORS

Experimental uncertainties exist in two basic categories, random and systematic. The former can be revealed through repeated measurements (e.g., averaging a number of independent measurements to approximate the true value being measured). However, systematic errors cannot be resolved through repeated measurements. These errors always exhibit some degree of uncertainty biased in one direction away from the true value being measured (e.g., a clock running consistently slow will always underestimate the true time in an experiment no matter how many trials are conducted) (Taylor, 1997).

Almost all measurements are subject to both systematic and random errors, but it is often possible to correct for both types of errors to reduce the final uncertainties. Random errors are identified through repeated measurements, and statistical methods exist to estimate how much the uncertainty is reduced with more sampling. A series of repeated measurements can be averaged, and this value ($\bar{x}$) is assumed to be more reliable than any individual measurement alone for determining the mean value. The standard deviation (σ_x) is a measure of the variance individual measurements deviate from the average and is a measure of the uncertainty of a single measurement. One standard deviation represents a 68% confidence interval that the true value of x lies somewhere between $\bar{x} \pm \sigma_x$. However, if these measurements are truly random and independent from each

other, the total uncertainty can be reduced by calculating the standard deviation of the mean ($\sigma_{\bar{x}}$), and is given by

$$\sigma_{\bar{x}} = \frac{\sigma_x}{\sqrt{N}},$$ (19)

where N is the number of measurements in the sample. In essence, (19) asserts that increasing the number of measurements reduces the randomness of independently measured values, and the error will eventually converge to zero with an infinite number of measurements. We can express any value x being measured with a random uncertainty $\sigma_{\bar{x}} = \delta x_{Ran}$ as

$$x = \bar{x} \pm \delta x_{Ran}.$$ (20)

Conversely, systematic errors cannot be resolved through increased sampling. This is because every measurement is biased in one direction from the true value, and affects the value $\bar{x}$ and not the degree of uncertainty associated with it. Systematic uncertainties are accounted for by the addition of a correction factor. Correction factors may range from simple coefficients to complex higher-order variables, denoted by δx_{Sys}. However, the integration of systematic uncertainty into (20) is somewhat complicated, and can have three forms:

$$x = \bar{x} + \delta_{Sys} \pm \delta_{Ran},$$ (21)

$$x = \bar{x} \pm \left(\delta x_{Sys} + \delta x_{Ran} \right),$$ (22)

or

$$x = \bar{x} \pm \sqrt{\left(\delta_{Sys} \right)^2 + \left(\delta_{Ran} \right)^2}.$$ (23)

Determining which of the above equations to use is no trivial matter, and it should also be noted there is no rigorous mathematical proof or justification in selection. However, with careful consideration to each source of error; (21), (22), and (23) can provide a reasonable estimation into the total uncertainty of our measurements. Systematic errors are inherently difficult to identify, since they require comparison to another (preferably more accurate) instrument. If one can conclusively determine than an anomalous systematic error is present with a

28

known value, a correction factor addition such as in (21) is an appropriate method to reduce the error. However, to be positively identified, a systematic error's magnitude must be significant enough to overcome other sources of error. As a result, there is another systematic uncertainty in the estimation of the correction factor. For this reason the systematic error in (21) is better represented by, $\delta x_{Sys} = CF \pm \delta x_{CF}$, where the correction factor (CF) of known value is differentiated from the uncertainties with determining that value. Equations (22) and (23) can be rewritten as

$$x = \bar{x} + CF \pm \left(\delta x_{Sys} + \delta x_{Ran} \right),$$ (24)

and

$$x = \bar{x} + CF \pm \sqrt{ \left(\delta_{Sys} \right)^2 + \left(\delta_{Ran} \right)^2 } \;.$$ (25)

The decision to use (24) or (25) largely depends on whether the error sources are independent or correlated. A simple sum of uncertainties, as in (24), represents the largest possible error associated with the measurement and would occur if these errors are 100% correlated. In many cases however, this may be a gross overestimation of uncertainty. If, for example, two sources of error are said to be no greater than 1%, the total uncertainty should be cumulative by use of (24) and equal 2%. However, if the given errors are said to have come from a normal distribution (i.e., 68% of all instruments have systematic errors better than or equal to 1%), and the errors are independent from each other, than (25) is more appropriate. In practice, exactly normal error distributions and complete independence between different error sources usually do not exist; however, we can assume these requirements are met closely enough to use the standard statistical techniques for computing a reasonably accurate estimates of the total measurement uncertainty. The quadratic sum in (25) reduces the margin of uncertainty provided by (24), but also acts to properly weight known sources of error. In some cases, sources of error will prove to be insignificant when compared with other sources in (24).

B.   INSTRUMENT ERRORS

Each instrument has an associated accuracy and precision that accompany its measurements. The manufacturer usually defines these properties as a result of rigorous testing in the laboratory. Accuracy is a description of how close a measurement is to the true value or reference value (systematic uncertainty). Precision, or sometimes known as reproducibility, is the degree to which multiple measurements differ from each other (random uncertainty). Total uncertainty is the combination of both accuracy and precision, and if defined by the manufacturer, may also include other sources of error in a variety of environmental conditions. In the case of both the radiosonde and tower sensors, the manufacturers provide total uncertainty and are listed in Chapter III.

According to Vaisala's radiosonde datasheet, the total accuracy includes repeatability, long-term stability, response time, effects due to measurement conditions (e.g., solar contamination), and effects from electronics. However, Vaisala also indicates that the temperature sensor performance depends on altitude. The response time is considerably faster 0.4 seconds at the surface compared to 2.5 seconds at 10 hPa. Repeatability is consistent at 0.15 C regardless of altitude, but reproducibility is much more dependable at the surface 0.2 C, where above 10 hPa reproducibility increases to 0.5 C. Vaisala engineered the radiosonde to operate within the entire vertical structure of the atmosphere, so claimed tolerances must account for all conditions. Our experiment was limited to five meters above the ground, so the expected instrument error is probably much less than the total error provided by Vaisala. Using the repeatability and reproducibility values for surface measurements an alternate instrument error of the radiosonde can be calculated

$$\delta\theta_{Rad} = \sqrt{0.2^2 + 0.15^2} = 0.25.$$

(26)

Another limitation of an instrument is the significant figures, or detail, used to read measurements. Both radiosonde and tower recorded measurements from all instruments to the hundredths place. Therefore, any measurement provided in

the experiment may be off by as much as ±0.005 units (e.g., a typical relative humidity recorded by tower sensor four might read 42.33%, and thus could actually be as high or low as 42.334% or 41.335%). The measurement of the seven tower sensor heights is also subject to error. These were originally reported in inches to the nearest ¼ inch by the assembly team. We can therefore expect tower heights recorded to have an accuracy of 0.125 inches. When converted to metric this translates into $\pm$ 0.318 cm.

C.   MEASUREMENT ERRORS

Uncertainties introduced as a result of instrument interpretation and experimental methods are considered measurement errors. There are two primary sources of measurement uncertainties in our experiment, altitude uncertainties while the aircraft is hovering, and contributions from the effects of an operating quad-copter (e.g., prop-wash and parcel mixing).

1.   Altitude Errors

Crucial to the experiment was hovering the InstantEye at a particular altitude, for enough time to adequately sample the atmosphere. However, achieving this proved challenging for several reasons. The aircraft maintained its position partially through its automatic control system, but also through operator control. Wind gusts created instability and altitude oscillations, as the control system tried to compensate. Altitude placement was also approximated by visual reference from the pilot since an accurate method of measurement would have interfered with the experiment. As a result, it is estimated that during the experiment, uncertainty in sUAS altitude could be as much as ±0.25 meters.

Our altitude error is significant because it directly affects the atmospheric values sampled. For instance, the temperature profile is a function of height and varies logarithmically in an unstable atmosphere. Therefore, an altitude increase of 0.25 meters will result in a potential temperature change not commensurate with an equal decrease in altitude from the same point. In Figure 11 is an example of how altitude uncertainty can affect the expected temperature

measurements. The red circles represent the altitude and mean potential temperature profile of the seven tower sensors during a flight that took place on May 6th. The dotted black line connecting the sensors is an interpolation of the measurements in log-space. The black "X" marks a distance 0.25 above and below each tower sensor located on the temperature profile, and the colored boxes are a visual representation of how much potential temperature uncertainty exists for the given change in altitude. It is easily observed that potential temperature uncertainty increases notably as altitude decreases in this very unstable surface layer situation.
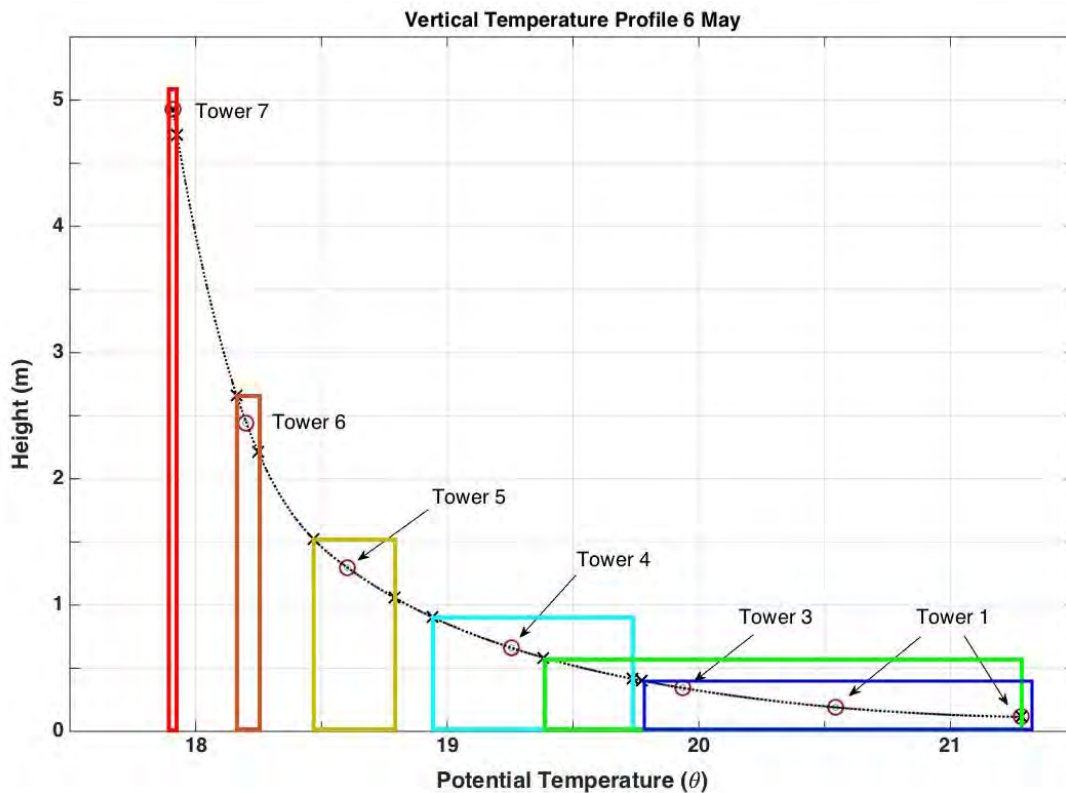
Figure 11.   Mean temperature profile with altitude error boxes

Note that in Figure 11, tower level one and two are labeled as a single tower sensor. This is again related to altitude uncertainty. The sensors at tower level one and two are 11 and 19 cm above the ground, respectively. This is well within the 25 cm estimated altitude error, and as a result it is nearly impossible to

differentiate a hover between the two levels. For this reason, levels one and two were consolidated for the subsequent analysis. Because the temperature profile is approximately linear between the lower two tower sensors, we can assume that the average height of sensor one and two (14 cm) will also correspond to the average temperature recorded by both instruments. For the remainder of this text, measurements indicated by tower sensor one refers to the average of both the lowest two tower sensors. Hence, tower sensor two's label is omitted from all figures and tables.

Up to this point, we have discussed two different types of uncertainty related to altitude in the experiment: uncertainty in measuring the tower heights, and uncertainty in the aircraft altitude. Total error with respect to altitude (z) can be expressed as

$$\delta z = \sqrt{\left(0.25\right)^2 + \left(3.18 x 10^{-2}\right)^2} \cong 0.25m \ , \tag{27}$$

where the first term is the radiosonde/sUAS height error, and the second term is the tower elevation height error. It is clear that the error contributed by the uncertainty in measuring tower height is negligible when compared to the uncertainty of the aircraft altitude.

Next, we must translate our error in altitude uncertainty into a useful parameter such as an uncertainty in potential temperature ($\delta\theta$). We will assume that our altitude uncertainty is random and normally distributed, since we were not purposely trying to deviate from the prescribed altitude level. In Figure 11, height is a function of temperature, and inside the altitude error boxes we can say that potential temperature is approximately linear. Averaging the two temperatures corresponding to δz, we get an expected value for Temperature with corresponding uncertainty

$$\overline{\theta} \pm \delta\theta \ . \tag{28}$$

However, this average temperature does not correspond to the temperature located at the tower sensor. Instead, the expected value measured by the

radiosonde is slightly above or below the average tower temperature, depending on the curvature or second derivative of the temperature profile. Likewise, magnitude and uncertainty are dependent on height. This means that each flight has unique uncertainties that need to be calculated for each tower level.

The magnitude of temperature error that is considered systematic is best represented as a correction factor (CF_{Alt}), while the random uncertainties are represented as $\delta\theta_{Alt}$. We are assuming that our altitude estimation is random, but we cannot say that all measurements taken are completely independent from one another; therefore, the N variable in (19) needs to be reduced from the value of the number of samples. This is because the aircraft takes time to recover from an altitude perturbation. If a wind gust brings the aircraft upward 0.25 m from a hovering state, it takes a few seconds for the operator and control circuitry to respond. During this time the sensor may make several measurements while elevated. The series of measurements made are related to a single altitude event; hence, they are not independent. We can say, however, that the group of measurements associated with the altitude event is independent from group associated with the previous and next altitude event. The application of (19) without grouping our samples underestimates the true random uncertainty associated with altitude. We know that the radiosonde records a sample every two seconds, and it is estimated that typical altitude perturbations require approximately three to five seconds to recover from. Therefore, each altitude event has a group of two measurements associated with it. Equation (19) can be rewritten for this particular example as

$$\sigma_{\bar{\theta}} = \frac{\sigma_\theta}{\sqrt{N/2}} \quad . \tag{29}$$

Although this method is quite subjective, it is a reasonable estimate of altitude groups, and provides a better value of uncertainty than if we had not grouped them at all.

2. Aircraft Errors

A second source of measurement uncertainty is the InstantEye platform. The four rotors spinning above the meteorological sensors likely have some effect on the surrounding air, but the extent to which this influences sensor measurement was not known before this research was performed. A major objective of this thesis work is to provide an answer to this question. This can only be achieved by accounting for all other sources of error, and incorporating the total uncertainty to the final analysis.

D. ENVIRONMENTAL ERRORS

The experiment was conducted outside in a non-controlled environment. As a result environmental influences further contributed to the total uncertainty in our measurements. Specifically, solar contamination and natural turbulent fluctuations were significant enough to be identified in the data.

1. Solar Contamination

Solar contamination is a significant problem with meteorological sensors. Direct exposure to the sun causes warming of the sensor's components, and in turn can affect the quality of measurements taken. The tower sensors were carefully designed to minimize solar influence through a double wall sensor enclosure and the installation of a solar shield, so it is assumed to be negligible. Conversely, both temperature and relative humidity are of particular concern on the RS92 since their sensing components are positioned on a metallic boom protruding outward from the main chassis directly exposed to the sun. Relative humidity is affected more by solar contamination due to its dependence on temperature. Several noteworthy attempts have been made to accurately account for solar contamination with the application of a relative humidity correction for the RS92 based on solar angle (Cady-Pereira 2008, Vömel 2007, Yoneyama 2008). While this correction is integrated into the RS92 software making it transparent to the user, the precision of the relative humidity sensor is

still inadequate for the conditions observed in our experiment, the details of which are further addressed in Chapter V.

The temperature probe is to a lesser degree affected by solar contamination, but still significant enough to contribute to the total uncertainty of temperature measurements. According to Vaisala (2010), the temperature sensor correction at sea level can be as much as 0.1 C at the maximum solar angle. This is also compensated for in the RS92 software, but requires two key assumptions in the operation of the radiosonde; the sensor boom is positioned at an angle, and it is attached to a weather balloon. Both of these measures ensure there is adequate ventilation over the sensor components.

A typical weather balloon ascends vertically at a velocity of about 5 m/s, and the air passing over the boom minimizes solar contamination effects. In our experiment, the entire radiosonde was positioned horizontally from its normal (balloon) operating position, negating the requirement for the boom to be angled. When the InstantEye was hovering there was no vertical motion of the sensor; however, eddies produced by the rotors assisted in the ventilation requirement. In the experiment, we were able maintain the InstantEye at ground level for approximately a minute with the rotors operating. We then turned the rotors off for an additional minute and observed an average temperature rise of 3.1 C. This is clear evidence that the propellers serve a key function in reducing solar contamination by providing ventilation to the RS92 sensors.

We then examined temperature observations with the radiosonde placed in the direct sunlight and compared them to those made in the shade. In both cases the InstantEye was hovering to ensure the rotors were providing sensor ventilation. In both observations no discernable difference in temperature measurements were observed, suggesting that ventilation is adequate over the sensor boom to reduce solar contamination to the manufacture's engineering specifications. This is confirmed in other studies conducted by Jauhiainen et al. (2014) and Moti (2014), where temperature comparison between day and night balloon soundings revealed a reproducibility of less than 0.1 C, with a standard

deviation of 0.02 C at the surface. We can safely conclude that the uncertainties contributed by solar contamination, while attached to an operating InstantEye, are sufficiently negligible that they do not need to be added to the manufacturer's claimed accuracy, which incorporates this error into its measurement algorithms.

2.   Turbulent Fluctuations

In an unstable atmosphere, it is expected to observe energy transfer from rising air parcels in the surface layer as a result of the ground being warmer than the atmosphere. These motions create localized turbulence and mixing, which can introduce random errors into our measurements of mean temperature values. Fortunately, these short-term variations can be reduced through sampling; however, one must first be able to isolate the contributions due to turbulence from all the other sources of noise. For this reason, it is quite difficult to develop a strategy to reduce uncertainty in our final measurements.

To get a feel for the data collected during the experiment, a time series plot is presented (Figure 12) over a fifteen-minute period for a flight conducted in May. This particular flight took place in the morning after sunrise in the presence of an unstable temperature profile. The reference tower measurements are displayed in multicolored lines with each color representing a unique sensor on the tower. Tower level one in dark blue is closest to the ground, and tower seven in red is the highest sensor on the tower. The tower sensors captured a series of peaks and troughs in potential temperature taking place over several minutes.
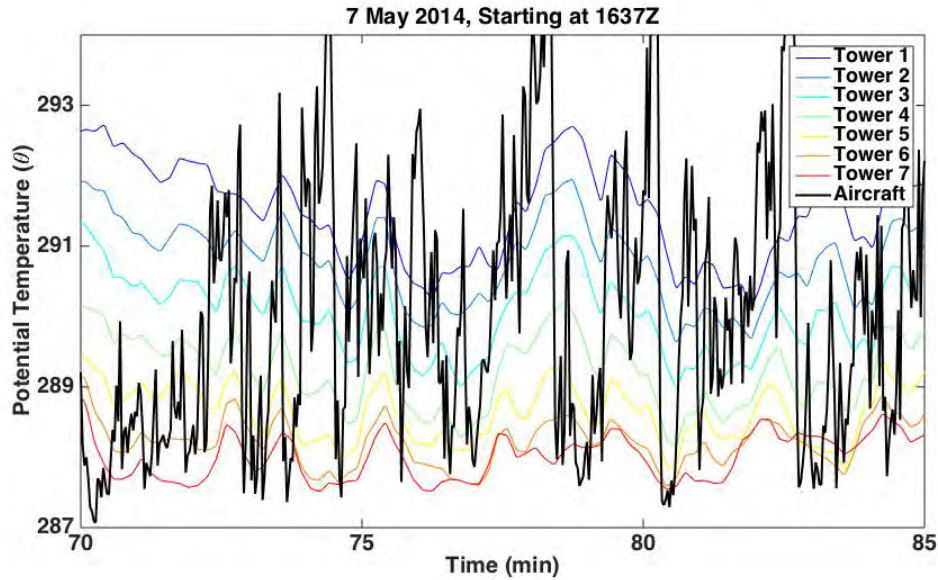
Figure 12.   Time series plot of temperature with large variations

Potential temperature captured by the radiosonde while in flight (black line) is overlaid on top of the data from the various tower sensors. This particular 15-minute section of flight was chosen as an example since the aircraft was in operation over the entire period, and was attempting to hover at altitudes corresponding to tower measurement levels. The variation in potential temperature observed by the radiosonde is quite extreme in both magnitude and time scale, and uncorrelated on small time scales with the variations captured by the tower. This can partially be explained by the fact that aircraft altitude and associated temperature error is absent from Figure 12. Another explanation can be related to the proximity of the tower and aircraft to each other. During a flight the aircraft was flown at a distance of around five to 10 meters away from the tower. This served to prevent a collision between the aircraft and tower, and also to prevent contamination of the tower sensors due to any prop-wash effects generated by the aircraft. Any turbulent eddies smaller than the separation distance produced uncorrelated temperature fluctuations.
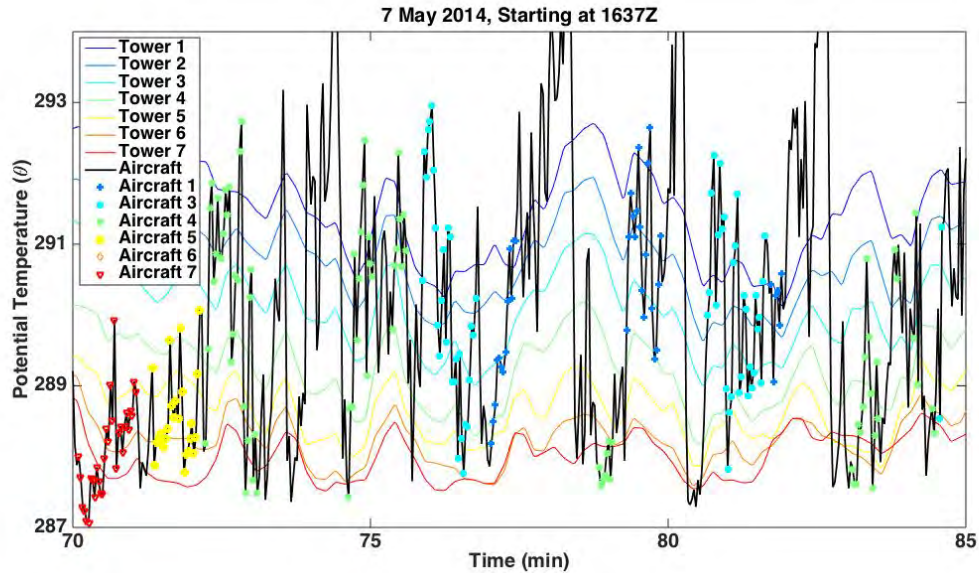
Figure 13.   Time series plot of potential temperature with aircraft heights

Figure 13 is the same time series as Figure 12 but with altitude data incorporated. The solid black line still represents the radiosonde's potential temperature record, but with the addition of color-coded data points. Each point is displayed with a unique shape and represents a hovering altitude. The color associated with the data is same color as the corresponding tower level (e.g., when the aircraft was said to be hovering at level five, all the recorded measurements are indicated by a yellow square—yellow being the color representing tower five).

There are portions of the radiosonde's profile in Figure 13 without accompanying altitude data. These reflect periods of altitude transition, or times when control of the aircraft was difficult. These data were rejected in the analysis since it is unclear where the aircraft was located at these times. However, when looking at the data of value (i.e., those points containing altitude information) the variability is still very large for a given hovering level. Since the tower sensors had less variability than the aircraft, there are three possible explanations: (1) This is a result of altitude variation, (2) the variations are natural in origin but are not adequately being captured by the tower sensors due to a slower

response time, or (3) the forces and motions of the aircraft rotors are driving large-scale variations.

The temperature sensors on both the tower and radiosonde have some key differences in sampling methods. The radiosonde uses a fast response capacitance sensor, which records a temperature reading every two seconds. The tower sensors use an RTD, which average over a 30-second time interval, recording temperature values every 10 seconds. By design, the tower temperature sensor will smooth out large short-term temperature fluctuations if present. To determine if the same variations recorded by the radiosonde were also present at the tower, a fast response thermocouple was installed at tower level four during the August and November JIFX flights. In doing so, the thermocouple is devoid of any altitude uncertainty or adverse effects contributed by the aircraft rotors. The thermocouple also records its temperature measurement every second, providing an improved sample rate over both the tower sensors and the radiosonde.

Figures 14 and 15 provide sample windows comparing the three different types of temperature sensors under two different conditions. The unstable atmosphere is presented in Figure 14, taking place during a very warm August afternoon. The stable atmosphere is shown in Figure 15, which took place on a cool November morning before sunrise. Note, due to a processing error, radiosonde data were only recorded to within 0.1 C for the stable profile. In both cases, large short-term variation in potential temperature is captured by both the thermocouple and radiosonde. The magnitude of variation observed in the unstable atmosphere is larger when compared to the stable atmosphere. More importantly, the radiosonde and thermocouple recorded temperature variations nearly identical in magnitude for both cases. Since there was no altitude or prop-wash uncertainty in the thermocouple measurements, the same fluctuations captured by the radiosonde must also be natural in origin. This is because any additional variations on the radiosonde measurements induced by other effects such as prop wash would be expected to cause higher variability. Other sources

of error included in the radiosonde's measurements are not easily identifiable in Figures 14 and 15. Figure 16 is a spectral plot of both the thermocouple and radiosonde showing similar results, including the -2/3 slope that is associated with turbulence in the inertial subrange. The apparent increase in spectral magnitude at the highest frequencies is due to aliasing; no filtering was performed. This similarity is further evidence that the radiosonde is observing fluctuations natural in origin. We would expect more high frequency variations if they were originating from the prop-wash.
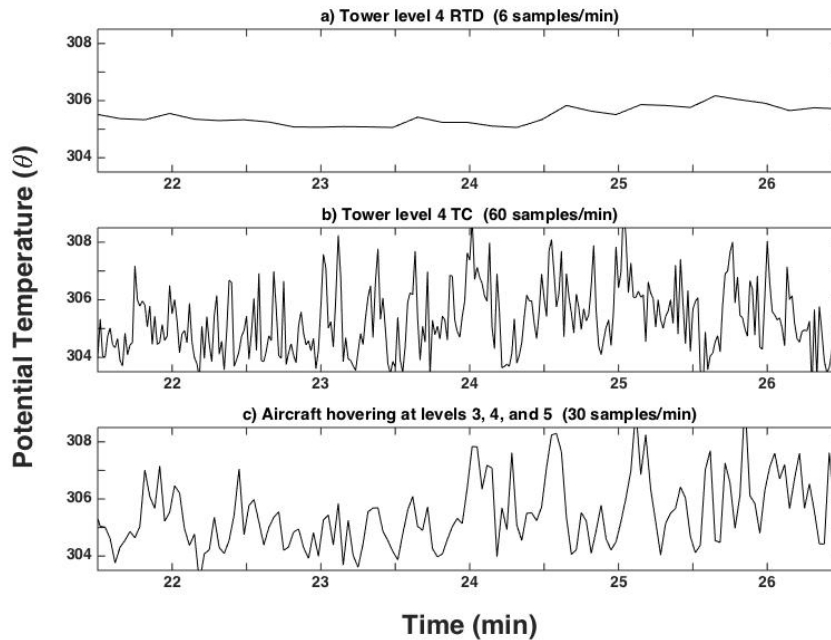
Figure 14. Time series of potential temperature (unstable conditions) taken on August 12th, 2014 starting at 2126Z, a) tower level four RTD, b) tower level four TC, and c) aircraft hovering at levels three, four, and five.
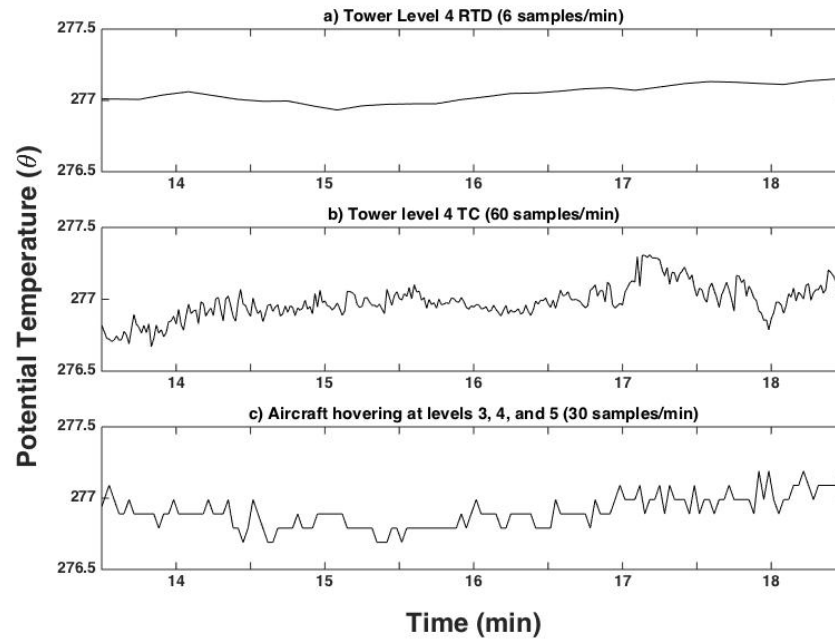
Figure 15.   Time series of potential temperature (stable conditions) taken
on November 5th, 2014 starting at 1413Z,
a) tower level four RTD, b) tower level four TC, and
c) aircraft hovering at levels three, four, and five.
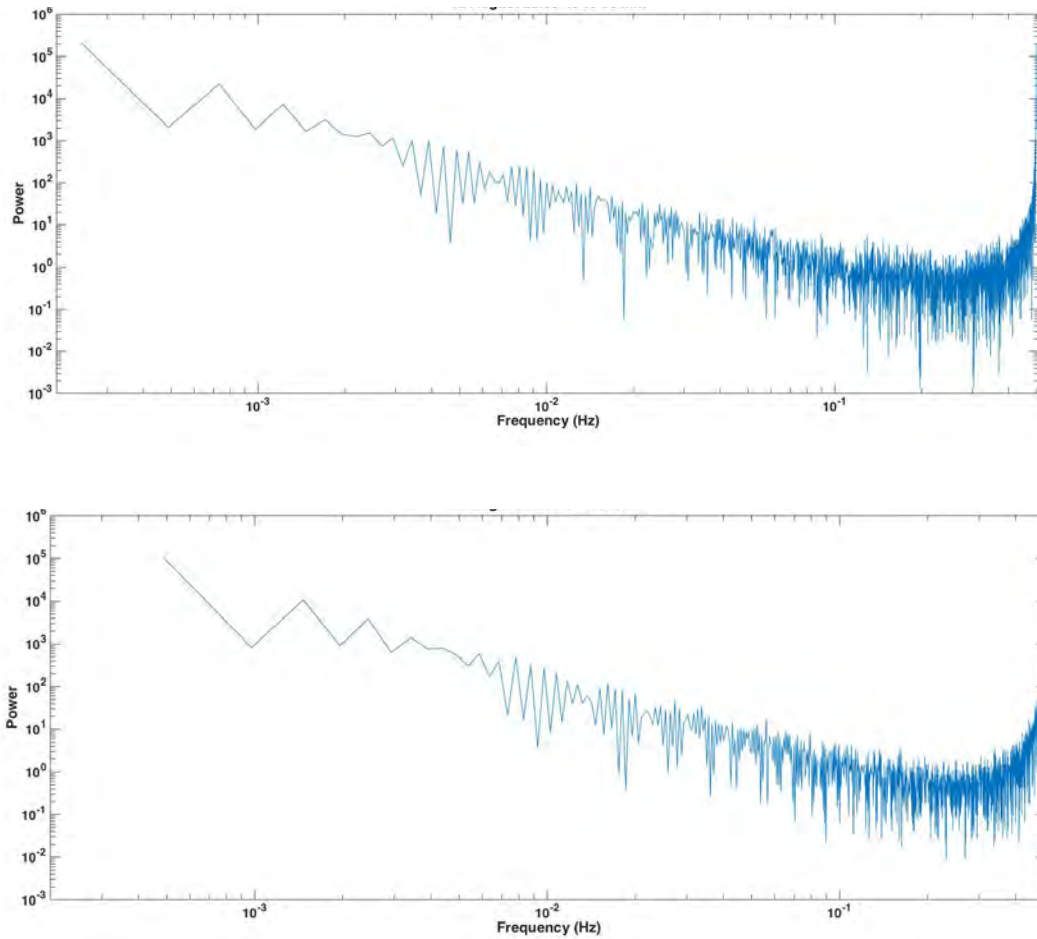
Figure 16. Spectral plot of potential temperature August 12th,
thermocouple (top) verses radiosonde (bottom).

The presence of natural temperature variations also reaffirms our choice in using the seven slow-response RTD tower sensors for analysis. At any instant in time, the measured temperature at the thermocouple will not likely match the temperature measured by the radiosonde as a result of turbulent fluctuations. The difference could be off by as much as four degrees, as in the example of Figure 14. In this case, a time-running average, as provided inherently by the tower RTD sensors is best to describe the mean state of the atmosphere in the presence of this natural variability. The seven sensors on the tower in effect perform this function through their longer response time averaging out short-term variations. This provides an accurate reference mean temperature for comparison with the radiosonde.

Since turbulent fluctuations are pseudo-random, their uncertainty can be reduced through sampling. However, determining the variation of fluctuations is particularly challenging in this experiment due to the absence of data. The measurements recorded by the radiosonde while in flight capture turbulent fluctuations as shown above, but also contain altitude and prop-wash uncertainty embedded within. To determine the variability of natural fluctuations an independent fast-response probe is required, and our thermocouple was installed late in the experiment. There are only three flights with fast-response data available, and four flights without.

Immediately following one flight in August we used the radiosonde to gather some turbulent variation data. During this test, the InstantEye was shut down and manually held next to the lowest five tower sensors for approximately one minute. This removed any unwanted altitude, prop-wash, or spatial uncertainty in the measurements when compared to each tower sensor. Tower levels six and seven were not included in the test because they were too high to reach and keep stable for consistent measurements. Table 4 summarizes those results.

Level	N	$\sigma_{\Delta\theta}$
5	30	0.58
4	30	1.03
3	30	1.15
1	47	1.21

Table 4.   Difference in potential temperature test results
(radiosonde–tower) with props off,
and held manually.

The results of the test demonstrate that standard deviation decreases with height and is in alignment with surface layer theory. According to an empirically derived study (Garratt 1992), temperature variations in the surface layer during unstable conditions can be represented as a function of height (z),

$$\frac{\sigma_\theta}{\theta^*} = 0.95\left(\frac{z}{-L}\right)^{-\frac{1}{3}}, \tag{30}$$

where θ^* is the temperature scaling parameter, and L is the Monin-Obukhov length scale. If we assume that turbulent fluctuations are consistent, then θ^* and L are by definition constant in the surface layer, so (30) can be represented as

$$\sigma_{\theta Turb} = cz^{-\frac{1}{3}}, \tag{31}$$

where c is a constant for a given θ^* and L. Equation (31) shows how variation is expected to diminish with height, and our test results confirm a close relationship. Therefore, not only do we require an independent fast-response sensor during each flight, one is also required at each level to accurately determine the variation of natural fluctuations. We fall well short of this requirement so must rely on analytic methods to account for these uncertainties.

We should also expand upon our independent test conducted at the lowest five tower levels to include the fast-response thermocouple. Looking at the difference between the thermocouple and tower level four for the entire flight, our sample size is increased to 6650 and the standard deviation of potential temperature difference between tower and thermocouple is 1.25 C. Since our test with the radiosonde was limited to 30 samples producing a standard deviation at level four of 1.03 C, it is clear that we need a larger sample size to adequately represent the variation of turbulent fluctuations. Knowing the heights of each tower level, and having sampled $\theta_{\theta 4_{Turb}} = 1.25$ C from the thermocouple, we can then solve for c in (27) and apply the equation to other levels. This helps resolve our turbulent fluctuation uncertainty at different heights, but does not account for the flights where the thermocouple was unavailable for a reference.

A larger unstable temperature gradient will produce greater temperature variability (Garratt 1992). Given this relationship, we can estimate the standard deviation of short-term temperature fluctuations by only knowing the difference in

temperature. This is possible since the tower was left to record measurements continuously for several days, and accumulated an abundance of data from the thermocouple and tower sensor four. Figure 17 shows the relationship between temperature gradient and variation. Over four days, the thermocouple was compared to the potential temperature recorded by tower sensor four. Standard deviation was calculated every 15 minutes using an hour window (3600 samples), and then plotted against the average temperature gradient recorded during that hour (tower one–tower seven). The results clearly show a linear relationship between the two variables, which can be represented by

$$\sigma_{\theta 4_{Turb}} = 0.40\left(\bar{\theta_1} - \bar{\theta_7}\right) + 0.05.$$ (32)
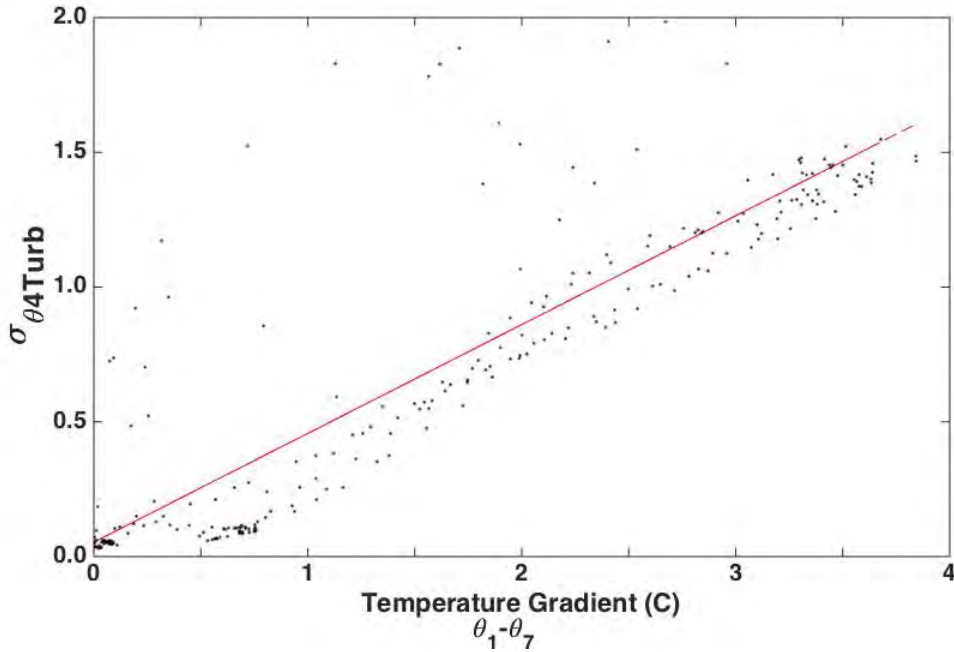
Figure 17.   Relationship between temperature gradient and standard deviation of the difference in potential temperature between the thermocouple and tower sensor 4

Using (28) we can generate a reasonable estimate of $\sigma_{\theta 4_{Turb}}$, the standard deviation due to turbulent fluctuations at level four. Equation (27) can then be used to estimate the variation at each level knowing only the average temperature gradient for unstable atmospheres. For stable atmospheres, we do

46

not expect to see variations as a function of height. Garratt confirms that a relationship between σ_θ and other parameters under stable conditions are uncertain. Under stable conditions we know that small variations appear in the data as shown in Figure 15, so we can assume similar variations were also present during the May 8th morning flight. For these reasons, we would be safe to assume similar variations at each tower level. Examining the uncertainty from stable conditions in the August and November data, 95% of $\sigma_{\theta 4_{Turb}}$ samples from the thermocouple remained below 0.37 C. This figure is probably larger than what actually occurred that morning, but gives us a safe value of uncertainty for analysis.

Similarly to our altitude uncertainty, we cannot assume that measurements with turbulent fluctuations are independent from each other. Each fluctuation requires time to pass through a parcel. We estimated that this time was about six seconds, or three measurements from the radiosonde. For turbulent fluctuations, Equation (19) can be rewritten as

$$\sigma_{\bar{\theta}Turb} = \frac{\sigma_\theta}{\sqrt{N/3}} \quad . \tag{33}$$

Tables 5 and 6 present the potential temperature gradients, uncertainties, and uncertainties in the mean used for calculation of errors associated with turbulent fluctuations.

Level	May 6	May 7	May 7	May 8	Aug 12	Aug 13	Nov 5
7	17.86	14.00	19.50	5.90	31.28	22.33	5.05
1	21.28	17.46	23.20	5.59	34.46	25.21	3.41
$\Delta\theta$	3.42	3.46	3.70	-0.31	3.18	2.88	-1.64

Table 5.   Average flight temperatures in C recorded
at levels one and seven

47

Level	May 6 $\Delta\theta = 3.42$		May 7 $\Delta\theta = 3.46$		May 7 $\Delta\theta = 3.70$		12 Aug $\Delta\theta = 3.18$		12 Aug $\Delta\theta = 2.88$	
	$\sigma_{\theta_{Turb}}$	$\sigma_{\bar{\theta}_{Turb}}$	$\sigma_{\theta_{Turb}}$	$\sigma_{\bar{\theta}_{Turb}}$	$\sigma_{\theta_{Turb}}$	$\sigma_{\bar{\theta}_{Turb}}$	$\sigma_{\theta_{Turb}}$	$\sigma_{\bar{\theta}_{Turb}}$	$\sigma_{\theta_{Turb}}$	$\sigma_{\bar{\theta}_{Turb}}$
7	0.73	0.13	0.74	0.17	0.79	0.11	0.68	0.10	0.62	0.15
6	0.93	0.13	0.94	0.15	1.00	0.16	0.86	0.14	0.79	0.16
5	1.14	0.17	1.16	0.18	1.23	0.24	1.07	0.15	0.97	0.16
4	1.43	0.33	1.45	0.15	1.55	0.22	1.34	0.16	1.22	0.16
3	1.79	0.47	1.81	0.24	1.93	0.38	1.67	0.22	1.52	0.36
1	2.40	1.86	2.43	0.35	2.59	0.39	2.24	0.52	2.04	0.35

Level	May 8 $\Delta\theta = -0.31$		Nov 5 $\Delta\theta = -1.64$	
	$\sigma_{\theta_{Turb}}$	$\sigma_{\bar{\theta}_{Turb}}$	$\sigma_{\theta_{Turb}}$	$\sigma_{\bar{\theta}_{Turb}}$
7	0.37	0.12	0.26	0.05
6	0.37	0.11	0.26	0.04
5	0.37	0.09	0.26	0.03
4	0.37	0.08	0.26	0.04
3	0.37	0.12	0.26	0.04
1	0.37	0.12	0.26	0.04

Table 6.   Estimated uncertainty in potential temperature variation $\left(\sigma_{\theta_{Turb}}\right)$, and estimated uncertainty in the mean $\left(\sigma_{\bar{\theta}_{Turb}}\right)$ due to turbulent fluctuations.

E.   BIAS ERRORS

Some of our data revealed evidence of the radiosonde being significantly biased as it was recorded during flight. In these cases, we chose to discard our results because of the large uncertainty. However, we only conducted two flights under stable conditions and both of these contained a large degree of bias. Because it is important to analyze both stable and unstable atmospheres we needed to correct for this uncertainty in the best way possible.
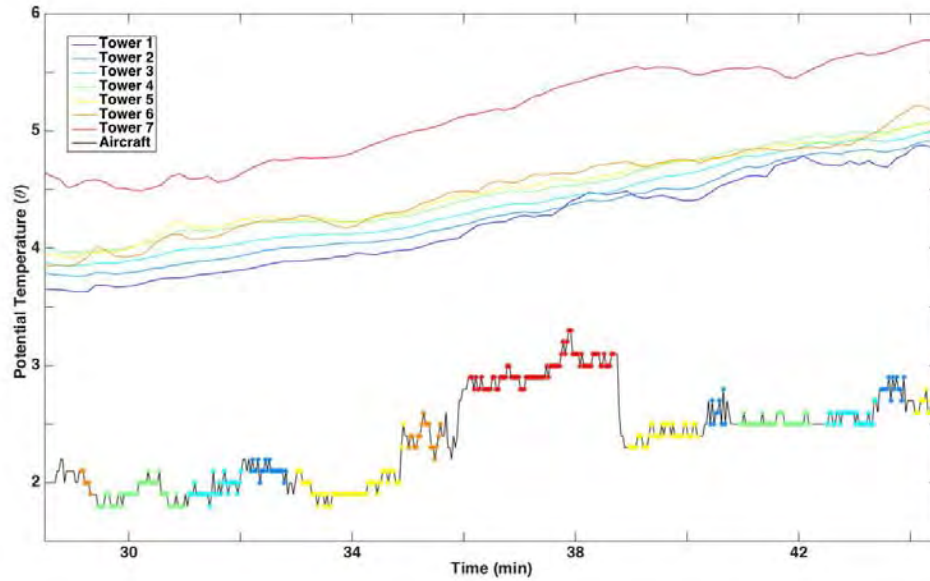
Figure 18.   Stable time series November 5th uncorrected
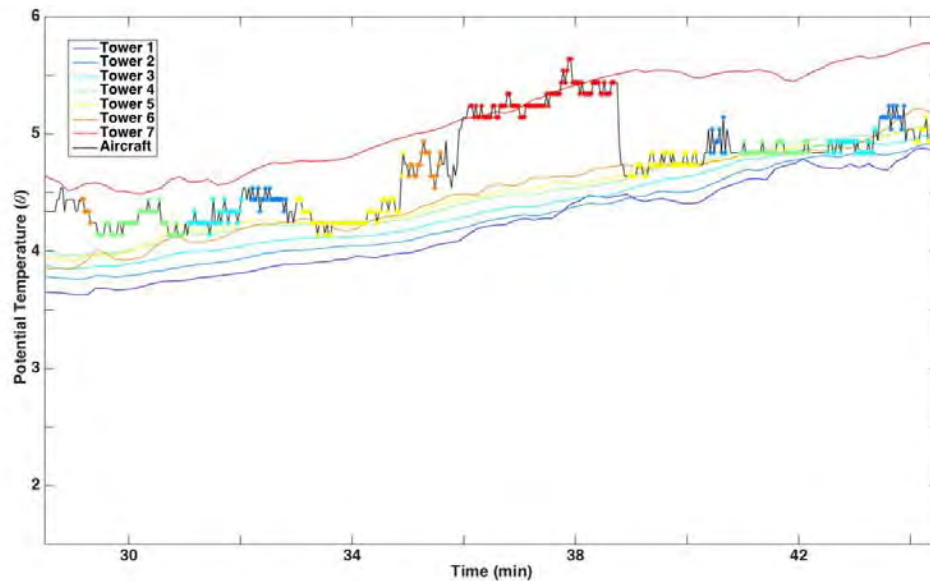
Figure 19.   Stable time series November 5th corrected for bias errors

Figures 18 and 19 provide an example of a bias error recorded on the morning of November 5th just before sunrise. The radiosonde temperature measurements are about 2.4 C cooler than the tower record as shown in Figure 18. The slope over the time series indicates that a gradual warming event is underway, and its being captured by both instruments suggests a simple

49

correction factor is an appropriate solution to the discrepancy. To accomplish this, we assumed temperatures recorded at level seven were most accurate due to a weaker gradient. The data were then fit to reflect temperatures recorded at level seven similar to those recorded by the tower instrument, as seen in red on Figure 19.

There are several possibilities why this bias was introduced. It could be that the radiosonde was not calibrated sufficiently. During the experiment radiosondes were used multiple times, and as a result could be subject to calibration issues. Another possibility could be the result of physical disturbance to the radiosonde. Our flights required some skill at keeping the aircraft airborne especially at lower levels, and the temperature sensor brushed against the ground during several "crashes" and hard landings over the course of the experiments. The data confirmed that on occasion a new bias error would occur after one of these events. It is uncertain if vibrations changed the internal calibration, or if the sensor was chemically or materially contaminated by accumulated debris in the form of soil or moisture.

F.   ERROR SUMMARY

After examining the various categories of uncertainty in our measurements, we can now formulate an acceptable method to interpret our measurements. We will focus on potential temperature since it is the primary parameter we are evaluating. Since we are comparing the temperature recorded by the radiosonde to the tower's measurement, we will normalize our measurements and perform statistical studies on the difference ($\Delta\theta$). Through averaging we can determine $\Delta\theta$ by

$$\Delta\theta = \overline{\Delta\theta} + CF_{Bias} + CF_{Alt} \pm \delta\theta \qquad (34)$$

where CF_{Bias} is the correction factor due to bias errors, CF_{Alt} is a correction factor due temperature offset related to altitude uncertainty. Tolerance is given by $\delta\theta$ defined as

$$\delta\theta = \sqrt{\delta\theta_{Rad}^2 + \delta\theta_{Twr}^2 + \delta\theta_{Alt}^2 + \delta\theta_{Turb}^2} , \qquad (35)$$

where $\delta\theta_{Rad}$ and $\delta\theta_{Twr}$ are the instrument errors associated with the radiosonde and tower, respectively, $\delta\theta_{Alt}$ is the uncertainty in temperature due to altitude, and $\delta\theta_{Turb}$ is the uncertainty related to turbulent fluctuations, all assumed to be independent. Equations (34) and (35) are then applied to the data set, formulating Table 7, providing total correction factors and uncertainty for each flight at each tower level.

Level	May 6 CF_{Total}	$\delta\theta$	May 7 CF_{Total}	$\delta\theta$	May 7 CF_{Total}	$\delta\theta$	12 Aug CF_{Total}	$\delta\theta$	12 Aug CF_{Total}	$\delta\theta$
7	-0.01	0.41	0.00	0.43	-0.01	0.41	0.00	0.40	0.00	0.42
6	0.00	0.41	0.00	0.42	0.00	0.42	0.16	0.42	-0.01	0.42
5	-0.02	0.43	-0.04	0.43	-0.01	0.46	0.03	0.42	0.01	0.42
4	-0.08	0.52	-0.10	0.42	-0.14	0.45	-0.34	0.43	-0.05	0.42
3	-0.39	0.64	-0.30	0.47	-0.56	0.58	-0.33	0.47	-0.37	0.56
1	0.39	1.96	0.51	0.53	0.48	0.56	1.06	0.71	0.53	0.54

Level	May 8 CF_{Total}	$\delta\theta$	Nov 5 CF_{Total}	$\delta\theta$
7	-0.75	0.41	2.59	0.39
6	-0.92	0.41	2.34	0.39
5	-0.72	0.40	2.35	0.39
4	-0.90	0.40	2.41	0.39
3	-0.90	0.41	2.40	0.40
1	-0.77	0.41	2.21	0.39

Table 7.　Total correction factor and uncertainty

THIS PAGE INTENTIONALLY LEFT BLANK

V.   ANALYSIS AND RESULTS

A.   HUMIDITY

Humidity is an important atmospheric property affecting the characteristics of EM propagation, and our analysis would not be complete without addressing this in our findings in the experiment. Unfortunately, due to the dry surface at Camp Roberts, specific humidity gradients (closely related to the vapor pressure, which controls EM refraction) were negligible during each of our flights, so performing the same type of analysis that was performed for potential temperature was not possible. Table 8 provides the mean specific humidity in g/kg recorded by the bottom six sensors for each of the flights. Relative humidity was the actual property measured by the sensors, but since it is dependent on temperature, relative humidity was converted to specific humidity, a conserved quantity described in Chapter II. The datalogger did not record humidity measurements from tower level seven so these data are absent. By examining the quantities depicted in Table 7, no obvious trends exist as a function of height. Differences between tower levels were also insignificant, and the maximum difference observed between any two tower levels was no greater than 0.50 g/kg for each of the flights.

Level	May 6	May 7	May 7	May 8	Aug 12	Aug 13	Aug 13	Nov 4	Nov 4	Nov 4	Nov 5	Nov 5
6	4.45	5.66	5.68	4.99	4.45	5.66	5.68	6.35	5.90	5.09	5.13	4.97
5	4.66	5.77	5.88	4.99	4.66	5.77	5.88	6.40	6.00	5.28	5.13	4.94
4	4.63	5.74	5.76	4.89	4.63	5.74	5.76	6.46	6.04	5.31	5.23	4.98
3	4.54	5.80	5.65	4.97	4.54	5.80	5.65	6.58	6.12	5.20	5.20	4.90
1	4.67	5.98	5.85	4.95	4.67	5.98	5.85	6.76	6.40	5.33	5.18	4.83
Maximum Difference	0.22	0.32	0.23	0.10	0.22	0.32	0.23	0.41	0.50	0.24	0.09	0.16

Table 8.   Mean values for specific humidity (g/kg) by tower level and flight

A result of relatively homogeneous moisture content is the inability of the radiosonde to differentiate between measurements made at different altitudes. Figure 20 depicts the relationship between relative humidity as a function of temperature and specific humidity in a standard atmosphere of 1000 hPa using typical values observed during the experiment. The accuracy of the radiosonde's relative humidity sensor is ±5%. Figure 20 demonstrates that a 5% uncertainty in relative humidity corresponds to an uncertainty in specific humidity, around 0.5 g/kg. Since our observed differences in absolute humidity were mostly less than 0.5 g/kg we cannot analyze humidity given the accuracy of the radiosonde and lack of substantial gradients. For these reasons, we will focus our analysis on temperature only. Because potential temperature and specific humidity are both scalar quantities that are conserved and not affected by the sUAS except by air movement, we believe that the sUAS effects on sampling (air movement from different levels and turbulence) is the same for specific humidity as for potential temperature.
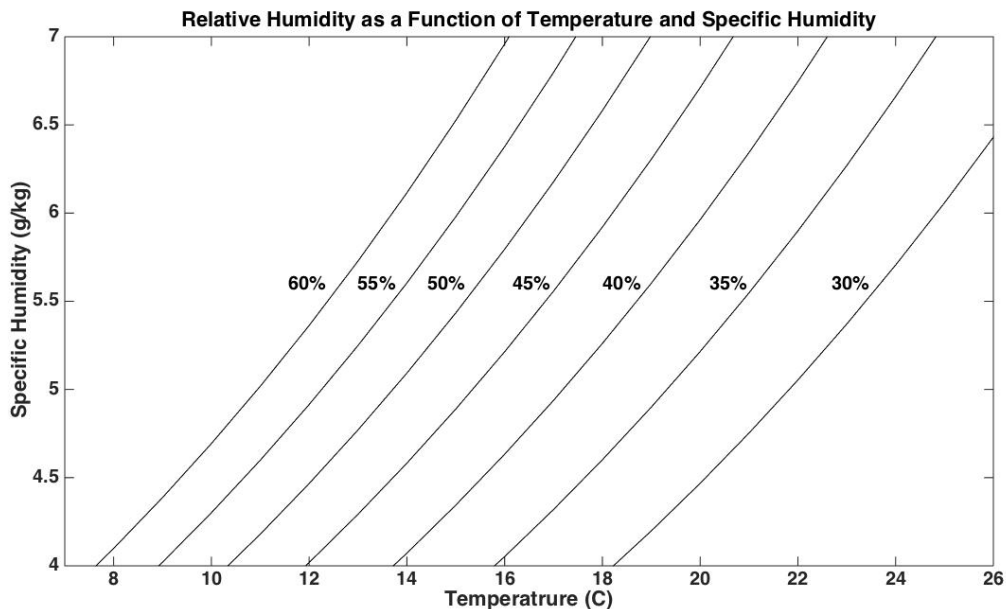
Figure 20.   Relative Humidity as a function of temperature and specific

B. POTENTIAL TEMPERATURE

We conducted a total of 12 flights during the three JIFX. Of these, we rejected five flights from our analysis due to obvious temperature bias errors or lack of sufficient data points. From the remaining seven flights, five were conducted in unstable conditions while the sun was present, and two were conducted in stable conditions before sunrise. The two flights conducted in a stable atmosphere also contained bias errors, but due to the absence of other reliable data, correction factors were used to account for errors as described in Chapter IV.

Our temperature analysis was only possible because we were able to compare measurements observed from the InstantEye to those observed from the tower at a corresponding altitude. We can mathematically represent our comparison by letting s represent the level at which the radiosonde was hovering, and t represent the tower level for each measurement i. The mean difference of potential temperature ($\Delta\theta$) then can be expressed as

$$\Delta\theta_{st} = \frac{1}{N}\sum_{i=1}^{N}\left(\theta_{si} - \theta_{ti}\right), \quad \text{where } s,t \in \{1,3,4,5,6,7\}, \tag{36}$$

where N is the total number of measurements observed during any single flight. When s and t are equal the expected value of $\Delta\theta_{st}$ should equal zero if no errors, environmental variations or sensor differences are present.

1. Unstable Profile

Results conducted from the five flights during unstable temperature conditions are shown in Table 9. In this particular table, s and t equal means that the radiosonde measurements are only being compared to the tower level in which the InstantEye was hovering adjacent to. The number of measurements is represented by N, $\Delta\bar{\theta}$ is the mean difference in potential temperature, $\sigma_{\Delta\theta}$ is the standard deviation of difference in potential temperature, and $\delta\theta$ is the

expected uncertainty of our calculation of $\Delta\bar{\theta}$ derived in Chapter IV. Note, that there were two separate flights that took place on May 7th.

a) $\Delta\theta$ 6 May

Level	N	$\Delta\bar{\theta}$	$\sigma_{\Delta\theta}$	$\delta\theta$
7	94	0.43	0.83	0.60
6	155	0.50	0.97	0.60
5	141	-0.10	0.84	0.61
4	55	0.47	1.08	0.68
3	44	0.16	1.05	0.77
1	5	0.08	0.44	2.01

d) $\Delta\theta$ 12 August

Level	N	$\Delta\bar{\theta}$	$\sigma_{\Delta\theta}$	$\delta\theta$
7	139	0.03	0.82	0.59
6	115	-0.03	0.82	0.60
5	158	0.10	0.87	0.60
4	202	-0.27	1.28	0.61
3	167	-0.44	1.59	0.64
1	56	0.25	1.29	0.83

b) $\Delta\theta$ 7 May

Level	N	$\Delta\bar{\theta}$	$\sigma_{\Delta\theta}$	$\delta\theta$
7	56	0.09	0.69	0.61
6	119	0.23	0.76	0.60
5	121	0.25	1.00	0.61
4	288	0.36	1.26	0.60
3	175	0.15	1.44	0.64
1	147	0.17	1.15	0.69

e) $\Delta\theta$ 13 August

Level	N	$\Delta\bar{\theta}$	$\sigma_{\Delta\theta}$	$\delta\theta$
7	52	0.17	0.49	0.60
6	69	-0.28	0.80	0.61
5	112	-0.11	1.02	0.61
4	180	0.18	1.08	0.60
3	53	-0.07	1.01	0.71
1	103	1.34	0.98	0.69

c) $\Delta\theta$ 7 May

Level	N	$\Delta\bar{\theta}$	$\sigma_{\Delta\theta}$	$\delta\theta$
7	158	-0.26	0.65	0.59
6	125	-0.23	0.86	0.60
5	81	-0.01	1.15	0.63
4	150	-0.19	1.11	0.62
3	76	0.22	1.36	0.72
1	135	0.44	1.36	0.71

Table 9.   Difference in potential temperature statistics of the radiosonde at hover compared to equivalent tower level in unstable conditions, a) May 6th, b) May 7th, c) May 7th, d) August 12th, and e) August 13th

There are some general trends observed from Table 9. First, each calculated mean $\Delta\bar{\theta}$ is well within its corresponding derived tolerances values $\delta\theta$ with the exception of August 13th at level one (shaded). This suggests that the InstantEye's effect on its radiosonde payload measurements was not detectable among the other sources of uncertainty and error. However, this tolerance is suspected to be high, since $\delta\theta$ was calculated using the total instrument error claimed by the factory, ±0.5 C. Recalculation of $\delta\theta$ with the alternate instrument error (26) derived in Chapter IV is shown in Table 10.

Level	6 May $\Delta\bar{\theta}$	6 May $\delta\theta$	7 May $\Delta\bar{\theta}$	7 May $\delta\theta$	7 May $\Delta\bar{\theta}$	7 May $\delta\theta$	12 Aug $\Delta\bar{\theta}$	12 Aug $\delta\theta$	13 Aug $\Delta\bar{\theta}$	13 Aug $\delta\theta$
7	0.43	0.41	0.09	0.43	-0.26	0.41	0.03	0.40	0.17	0.42
6	0.50	0.41	0.23	0.42	-0.23	0.42	-0.03	0.42	-0.28	0.42
5	-0.10	0.43	0.25	0.43	-0.01	0.46	0.10	0.42	-0.11	0.42
4	0.47	0.52	0.36	0.42	-0.19	0.45	-0.27	0.43	0.18	0.42
3	0.16	0.64	0.15	0.47	0.22	0.58	-0.44	0.47	-0.07	0.56
1	0.08	1.96	0.17	0.53	0.44	0.56	0.25	0.71	1.34	0.54

Table 10.   Mean difference in potential temperature between the radiosonde at hover compared to equivalent tower level in unstable conditions with alternate radiosonde instrument error

With a smaller tolerance for uncertainty, levels six and seven are now suspect measurements for the May 6th flight, but this is not a reoccurring trend for other flights. Most of the mean potential temperature values still remain within our expected tolerance. Our results still suggest that InstantEye contamination of potential temperature measurements is undetectable given our equipment and environment.

Another general trend observed from Table 9 is a decrease in the radiosonde temperature measurement variation ($\sigma_{\Delta\theta}$) with respect to height. This means that the accuracy of our measurements is greatly improved at the highest tower levels. This can be explained by the decreasing temperature gradient at

higher levels, as well as the related reduction in turbulent fluctuations as the aircraft moves away from the surface. The combination of these two factors also reduces our expected tolerance from the error Equation (35) as altitude uncertainty and fluctuations become increasingly insignificant above five meters, leaving instrument errors as the primary source of measurement uncertainty. If only instrument errors are considered, (35) would equal 0.39 C, and Table 10 indicates that $\delta\theta$ is converging to a number very close this value at tower level seven (4.93 m above the surface).

We suspect that the prop-wash effects would cause the sampled air parcels to come from a different level than the actually location of the sUAS. To quantify this scenario, Figure 21 is presented showing the mean radiosonde measurements compared to every other tower level. For instance, the mean potential temperature observed by the radiosonde while hovering at level four, can be compared with all six mean tower observations. The diagonal from bottom left to upper right are the figures $\Delta\bar{\theta}$ from Table 10, s and t being equal. Figure 21 is color-coded corresponding to the magnitude of mean potential temperature difference, and the column containing the value closest to zero is circled. Since the radiosonde measurements were subtracted from the tower's measurements, a positive value indicates the radiosonde is on average measuring warmer temperatures than the tower it is being compared to. Likewise, negative values indicate the radiosonde is measuring on average cooler temperatures than the tower sensor it is being compared to.

When examining each column of Figure 21, the $\Delta\bar{\theta}$ value closest to zero is an important location since it corresponds to the tower level and altitude. The zero point within the column implies that the mean air being sampled is originating from this altitude. One would expect to observe the mean difference closest to zero when s and t are equal (i.e., along the diagonal) if there is no influence from the InstantEye on vertical displacement of the sampled air. The circles in Figure 21 correspond to the tower levels closest to the zero value. This implies that circles above the diagonal are sampling air being pulled down from

the rotors, originating from a higher altitude. Conversely, circles below the diagonal imply that the mean air sampled is being pulled up from below as a result of rotor motions. The latter could occur if air is recirculated upward around the downwash. Circles along the diagonal suggest that the average air sampled is not originating from elsewhere, but is consistent with the atmosphere at its hovering altitude.
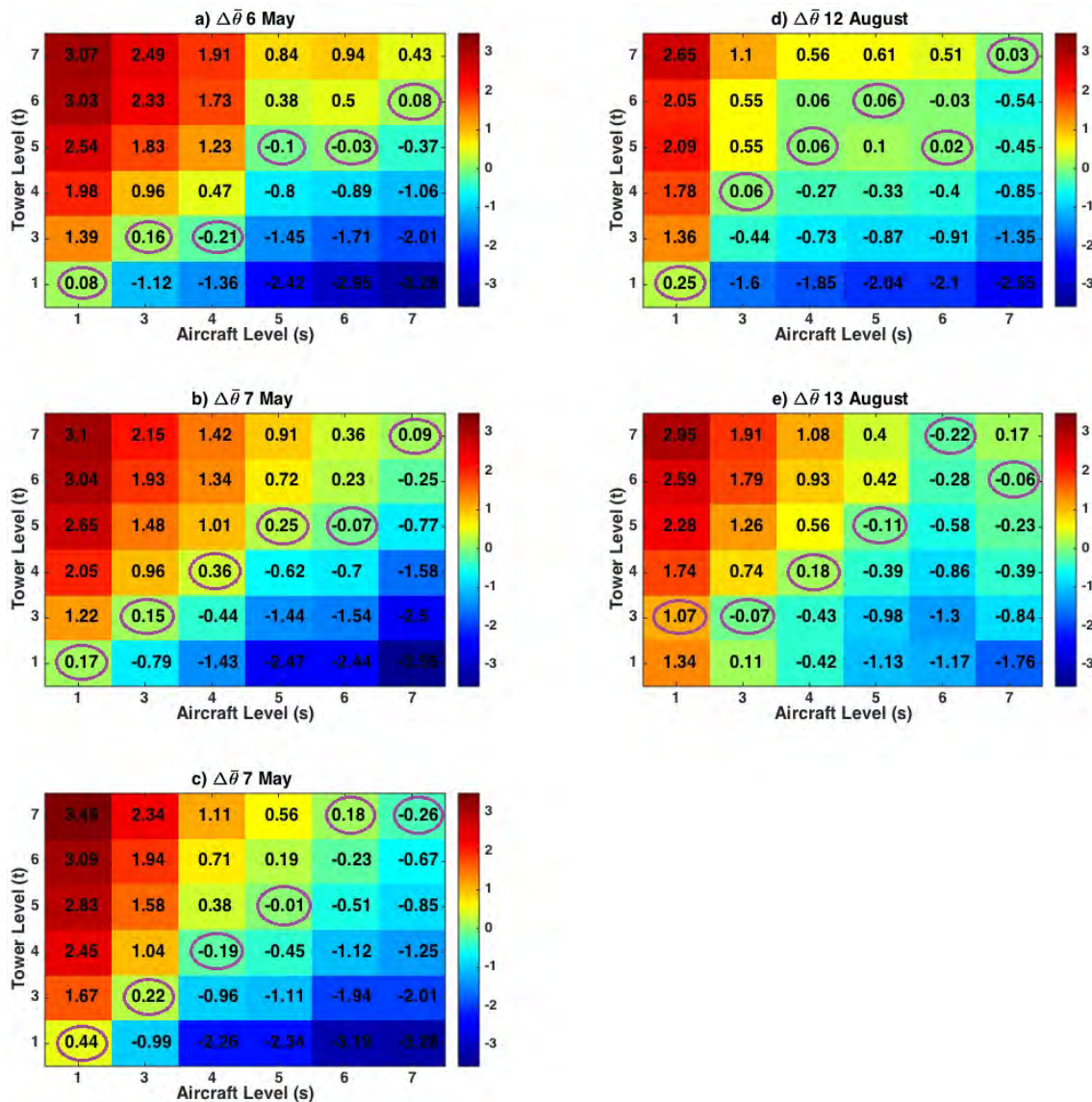

Figure 21.   Mean potential temperature difference, radiosonde (s) compared to each tower sensor (t).

59

Figure 21 illustrates that the potential temperatures from the tower and radiosonde match quite well along the diagonal, meaning the air being sampled has not been mechanically mixed sufficiently to significantly affect the mean values. Table 11 summarizes the positions of the circles corresponding to closest zero value in Figure 21. Each level is tallied into three categories; above, below, or on target (i.e., on the diagonal), totaling five for each of the separate flights. With the exception of level six, most levels indicate a strong tendency for the radiosonde to sample air similar to its corresponding tower level. Where this is not true, differences in $\Delta\bar{\theta}$ are slight, and a pattern cannot be established. There is no evidence at any altitude that the radiosonde tends to sample air above or below the rotor blades when averaged over a period of time. This is somewhat surprising as one might expect that the sampled air would always come from above the sUAS. It appears that some air that was pushed down by the props is recirculated back up outside of the downwash zone and brings some lower air up with it.

Level	1	3	4	5	6	7
Above	1	1	1	1	2	--
On Target	4	4	3	4	0	3
Below	--	0	1	0	3	2

Table 11.   Tally of mean potential temperature difference above, below, or on target with respective tower level.

2.   Stable Profile

There were only two flights conducted in the presence of a stable temperature profile. For this reason, the data for these flights were not rejected due to bias errors prevalent in the time series, but instead correction factors were applied. This creates difficulties in determining where the sample air comes from, since consistent sampling of air above or below would also create biases in the temperature. But we can look at the overall characteristics of the comparisons, even if the correction factor may not be exact. Results for the two flights are

summarized in Table 12, with the measurement uncertainty ($\delta\theta$) calculated with the smaller radiosonde instrument error.

Level	N	$\Delta\bar{\theta}$	$\sigma_{\Delta\theta}$	$\delta\theta$	Level	N	$\Delta\bar{\theta}$	$\sigma_{\Delta\theta}$	$\delta\theta$
		a) $\Delta\theta$ 8 May					b) $\Delta\theta$ 5 November		
7	31	0.05	0.12	0.41	7	97	0.00	0.09	0.39
6	34	0.25	0.25	0.41	6	106	0.47	0.15	0.39
5	52	0.01	0.13	0.40	5	216	0.03	0.25	0.39
4	64	0.05	0.06	0.40	4	132	0.10	0.12	0.39
3	27	0.18	0.12	0.41	3	108	0.20	0.19	0.40
1	28	0.15	0.06	0.41	1	131	0.76	0.39	0.39

Table 12.   Difference in potential temperature statistics of the radiosonde at hover compared to equivalent tower level in stable conditions, a) May 8th, b) November 5th

The differences in potential temperature are within the expected uncertainties, the exceptions being level one and six on November 5th. Note that the sample size from the flight on May 8th is much smaller than November's, due to limited flight time before sunrise. A smaller sample size may be insufficient to determine accurate means.

Unlike the unstable profile, there is no evidence that uncertainty in our measurements ($\sigma_{\Delta\theta}$) decreases with height. Also the expected variation of our measurements ($\delta\theta$) remains approximately constant in a stable profile. This is explained by reduced turbulent fluctuations that do not vary with height (discussed in Chapter IV) and a smaller temperature gradient resulting in less altitude-temperature uncertainty. The error tolerance is primarily from instrument errors, which will not reduce further. Similar to the unstable profile analysis above, a comparison of the radiosonde's mean potential temperature to each tower level is presented in Figure 22.
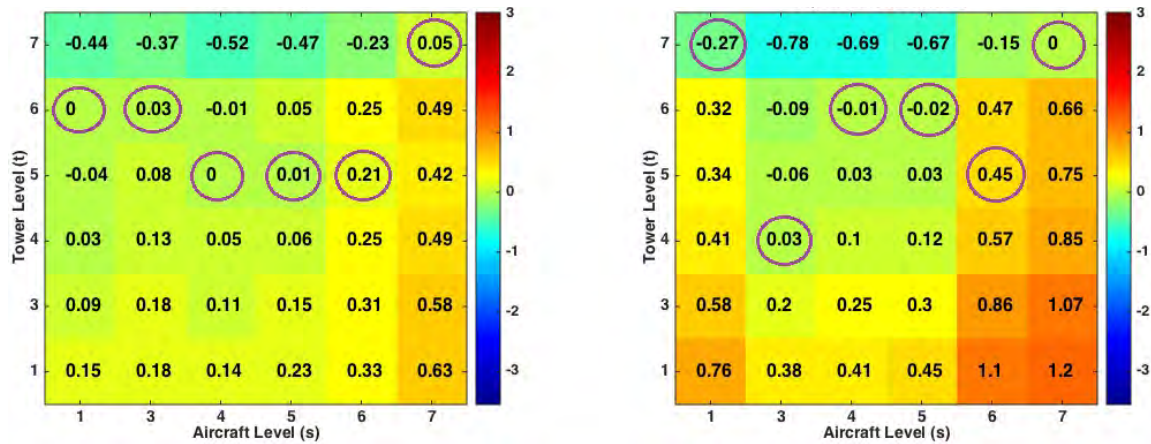
Figure 22.   Mean potential temperature difference between the radiosonde hovering at a particular level compared to each tower sensor for two separate flights in stable conditions, a) May 8th, b) November 5th

Again, the circles in Figure 22 represent the minimum absolute difference in potential temperature, and their arrangement is not along the diagonal as they were in Figure 21. Furthermore, choosing a value of $\Delta\bar{\theta}$ closest to zero is almost futile, because there exist several values very close (±0.1 C) to zero within a column. Most of the $\Delta\bar{\theta}$ values in Figure 22 also fall within their expected uncertainties, approximately 0.40 C.

As expected, the difference in potential temperature at tower level seven compared to the radiosonde hovering at seven is near zero. This is because the bias correction factors were formulated to ensure this was the case. There is clear evidence from Figure 19 in Chapter IV that a distinct temperature gradient is observed by the radiosonde between levels seven and five, but not at the lower levels. This can again be verified by column seven of Figure 22, indicating a distinction between observations taken at level seven compared to air sampled by the tower below it.

Our results also indicate that, below level seven, the radiosonde appeared to sample a layer of uniform temperature, even though we know a gradient

actually was present. Figures 19 and 22 illustrate the difficulty in differentiating the measurements taken while the radiosonde was hovering at levels five, four, three, or one. This can be explained by the InstantEye's prop-wash forcing the atmosphere to mix below level seven. Since the atmosphere is stable, and the lower levels are cooler than the upper layers, a major source of heat energy is absent from the surface to restore equilibrium to the local parcel of air the InstantEye is operating in. In this scenario, advection from adjacent air carried by the wind is the dominant force to restore equilibrium. However, it appears that the wind was too light (<3kts) during the morning flights to negate the mixing effects of the InstantEye.

When a stable temperature layer is mixed the cooler air on the surface will become warmer, and the warmer air aloft will become cooler; Table 12 shows this happening. In both cases $\Delta\bar{\theta}$ equals zero around level five. Below level five, $\Delta\bar{\theta}$ gradually increases, meaning the mean temperature observed by the radiosonde is warmer than mean temperature observed by the lower tower levels. Figure 23 depicts the mean potential temperature profile for the flight on November 5th. While the aircraft is hovering, the props force aloft air downward, displacing and mixing with the ambient and lower air. If the air being forced down confronts a boundary, in this case the surface, displacement and mixing are strengthened both laterally and upward since downward motion is limited and mass must be conserved. In the bottom five levels we observe a relatively homogeneous atmosphere, air is being forced from aloft near level six and mixing the lower levels. This explains the unusually high observed mean potential temperature at level one in Table 12.

The temperature gradient between levels five and six are approximately neutral in Figure 23. This prevents a drastic change in $\Delta\bar{\theta}$ while hovering at level five, since the air aloft is of similar temperature. However, the temperature gradient between levels six and seven is steeper. At some altitude above level six there is an inflection point and steepening temperature gradient, though it is not apparent from our data where it is. The surface is no longer as restrictive to

flow as it was while hovering at lower levels, so mixing is predominantly occurring between levels five, six, and the warmer layer aloft. This explains the 0.46 C warmer than expected $\Delta\bar{\theta}$ at level six in Table 12, suggesting the air is originating as high as 2 meters above the InstantEye.
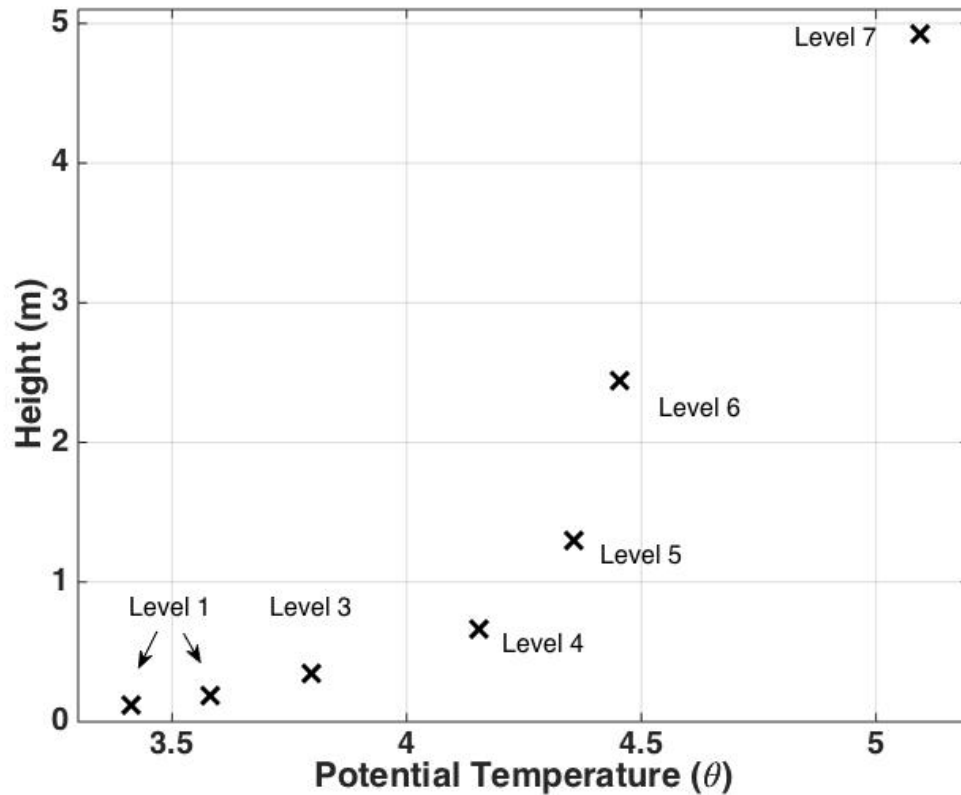
Figure 23.   Mean potential temperature height profile (first 15 minutes) observed from the tower sensors November 5th in (stable conditions)

3.   Turbulent Fluctuations

Our contrasting results between temperature measurements taken in stable and unstable atmospheres require a revisit to temperature fluctuations. We observed that in the presence of strong turbulent fluctuations, the prop-wash was on average an insignificant factor for temperature measurement accuracy.

However, in the presence of weak turbulent fluctuations, average temperature measurements indicate the action of the rotors are introducing contamination by mixing the vertical air column. Table 13 is a comparison of the standard deviation of the mean potential temperature observed with the expected standard deviation contributed solely by turbulent fluctuations. Greyed boxes indicate the observed variations in temperature measurements exceed those expected from turbulent fluctuations.

Level	May 6 $\sigma_{\Delta\theta}$	May 6 $\sigma_{\theta Turb}$	May 7 $\sigma_{\Delta\theta}$	May 7 $\sigma_{\theta Turb}$	May 7 $\sigma_{\Delta\theta}$	May 7 $\sigma_{\theta Turb}$	12 Aug $\sigma_{\Delta\theta}$	12 Aug $\sigma_{\theta Turb}$	13 Aug $\sigma_{\Delta\theta}$	13 Aug $\sigma_{\theta Turb}$
7	0.83	0.73	0.69	0.74	0.65	0.79	0.82	0.68	0.49	0.62
6	0.97	0.93	0.76	0.94	0.86	1.00	0.82	0.86	0.80	0.79
5	0.84	1.14	1.00	1.16	1.15	1.23	0.87	1.07	1.02	0.97
4	1.08	1.43	1.26	1.45	1.11	1.55	1.28	1.34	1.08	1.22
3	1.05	1.79	1.44	1.81	1.36	1.93	1.59	1.67	1.01	1.52
1	0.44	2.40	1.15	2.43	1.36	2.59	1.29	2.24	0.98	2.04

Level	May 8 $\sigma_{\Delta\theta}$	May 8 $\sigma_{\theta Turb}$	Nov 5 $\sigma_{\Delta\theta}$	Nov 5 $\sigma_{\theta Turb}$
7	0.12	0.37	0.09	0.26
6	0.25	0.37	0.15	0.26
5	0.13	0.37	0.25	0.26
4	0.06	0.37	0.12	0.26
3	0.12	0.37	0.19	0.26
1	0.06	0.37	0.39	0.26

Table 13. Standard deviation of mean potential temperature observed $\left(\sigma_{\Delta\theta}\right)$, and expected standard deviation due to turbulent fluctuations $\left(\sigma_{\theta Turb}\right)$

In the presence of an unstable atmosphere we expect to see variations in temperature due to turbulent fluctuations; strong near the surface and decreasing with height. This relationship is observed in our measurements. However, most of the variation in our observations is less than what was expected, suggesting that the InstantEye is reducing variations caused by turbulent fluctuations. It is only at levels five, six, and seven that we observe the variation of our measurements exceeding those expected from turbulent fluctuations, thus other forces are contributing to uncertainty at higher altitudes. Also note that as our observations approach the surface variations in measurements become larger, but not to extent we expect from the growing contributions due to turbulent fluctuations. Furthermore, the growing uncertainty of our measurements produces an anomalous reversal at level one where $\sigma_{\Delta\theta}$ is usually less than level three.

For the flights in a stable temperature profile, uncertainty from turbulent fluctuations has no height dependency, so we assume they remain constant with elevation. The uncertainties in our measurements are smaller than what we observed for the unstable case due to smaller magnitude gradients and turbulent fluctuations, but an unusually large uncertainty is observed at level one for the November flight. A similar finding did not appear in the May flight, but this may be related to the limited number of samples taken (28 in May versus 121 in November). This result shows the InstantEye making a strong contribution to temperature measurement variations near the surface.

Our findings in potential temperature observations indicate that the InstantEye contributes to measurement uncertainty while hovering, and this contribution is greatest near the ground. Turbulent fluctuations were present in every flight, but the InstantEye's contamination assisted in counteracting this source of uncertainty.

As the InstantEye gains altitude, variations due to turbulent fluctuations decrease in an unstable atmosphere, and eventually the InstantEye's

66

contributions to measurement uncertainty become apparent. This explains why on August 13, the radiosonde measured more variation than was expected due to fluctuations at level five (Table 13). The temperature gradient on this day was the least of the five unstable flights, and in turn variations from turbulent fluctuations were also the least. On this day the InstantEye's effect on measurement uncertainty was observed at a lower level than usual. Note how on both May 7th flights, the temperature gradient was the largest, and turbulent fluctuation variations were also the largest of the seven unstable flights. On these flights, fluctuations were so strong that the InstantEye could not overpower them at level seven.

As the InstantEye descends to the layer just above the surface (level one) prop-wash contamination effects become stronger, as do turbulent fluctuations. In the stable case fluctuations were comparatively small, so variations in the measurements hovering at level one was dominated by InstantEye contamination. Whereas in the unstable flights turbulent fluctuations were strongest at level one, but the amplified effect from the InstantEye helped to reduce measurement variations considerably. In the case of August 13th the observed variation in temperature measurements was smaller than the other flights at level one. The reduced affect from natural fluctuations together with the amplified affect from the InstantEye established a close to equilibrium state. Evidence of this can be found in the anomalous rise of potential temperature difference (Figure 21) at level one. The surface's energy transfer is restricted causing the air in the vicinity of the InstantEye to warm.

C.   PRESSURE

Another important atmospheric parameter for meteorological and EM prediction is pressure. The pressure differential across a rotor plane generates lift (Layton 1984), and therefore we should expect to observe higher pressure from the radiosonde since it is positioned beneath the rotor plane. To quantify the magnitude of pressure error due to lift, we examined measurements taken during

the August 13th flight. Near the end of the flight we hovered for a period of time at the lowest six levels. Shortly after, we turned the aircraft off and held the radiosonde at the lowest six tower levels for a period of time. Level seven was too high to reach by hand. Figure 24 and Table 14 illustrate the data collected and the results.
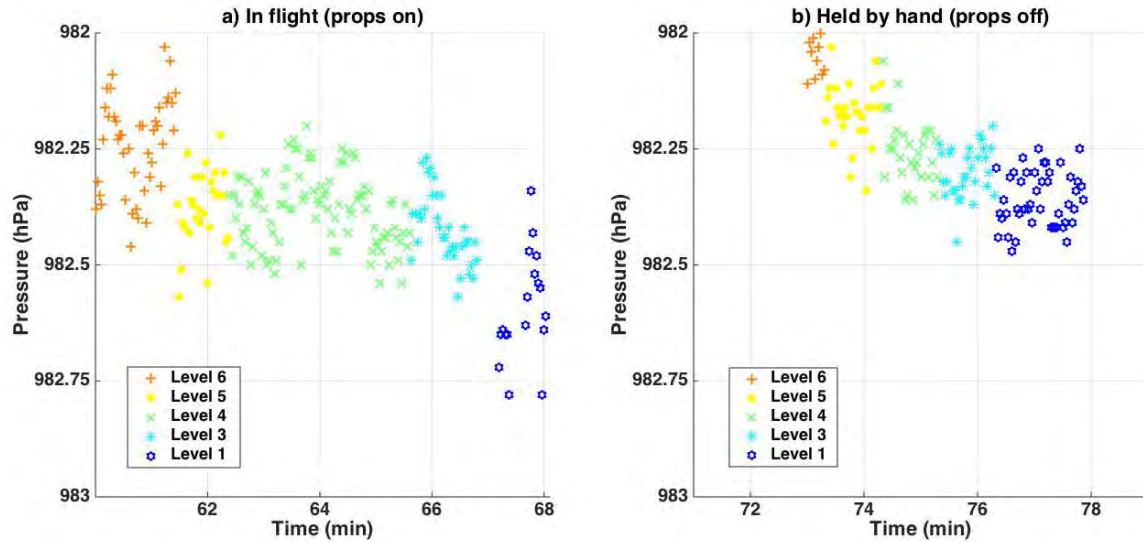

Figure 24.   Dynamic pressure captured by the radiosonde on August 13th, a) InstantEye in flight, b) InstantEye not in flight (held at each level by hand).

Level	In Flight		Held by hand		$\Delta\bar{P}$
	$\bar{P}$	σ_P	$\bar{P}$	σ_P	
6	982.23	0.11	982.05	0.04	0.18
5	982.38	0.08	982.17	0.07	0.21
4	982.38	0.08	982.25	0.07	0.13
3	982.42	0.08	982.30	0.05	0.12
1	982.59	0.12	982.36	0.06	0.23

Table 14.   Mean, standard deviation, and mean difference of pressure recorded by the radiosonde August 13th, with and without rotors operating.

The data points in Figure 24 exhibit a degree of uncertainty for both cases. When the radiosonde was held by hand, there is no altitude uncertainty, and since we are only comparing results against the same instrument, we only need the radiosonde's instrument error to determine the expected uncertainty. Vaisala claims that at the surface repeatability of the pressure sensor is within 0.4 hPa assuming a 95% confidence interval (i.e., $\pm 2\sigma$ where $\sigma = 0.1$ hPa), and the data presented in Figure 24b as well as Table 14 indicate this agrees with the present observations.

The radiosonde in flight must account for altitude uncertainty in addition to instrument error. We estimated our altitude error to be ±0.25 m, which translates into an expected pressure uncertainty of 0.03 hPa, since the expected rate of pressure change with elevation in a standard dry atmosphere is approximately 0.12 hPa/m (Petty 2008). Total pressure uncertainty from the radiosonde in flight becomes

$$\delta P = \sqrt{0.1^2 + 0.03^2} \cong 0.104 \text{ hPa.} \tag{37}$$

This is a negligible difference, and while in flight, all but the pressure measurements from levels six and one remained within expected uncertainty.

The differences between mean pressures values ($\Delta \bar{P}$) in Table 14 suggest that there is a constant pressure bias from the InstantEye ranging from 0.12–0.23 hPa. This corresponds to a 1–2 m change in altitude, and there is no observable relationship between pressure bias and tower level. In a similar experiment, Dr. Peter Guest of the Naval Postgraduate School found pressure bias to increase near the surface (Figure 25) while in flight due to ground-effect. This effect became apparent at about 1.3 m, and the maximum mean bias was observed to be 0.6 hPa just above the surface near 16 cm (Guest and Machado 2015).

Altitude oscillations during our flight may explain our inability to recreate Figure 25. Above we showed that expected pressure change due to altitude variations are negligible with an uncertainty of ±0.25 m, but we did not take into

account the InstantEye's effect on pressure beneath the rotors. The aircraft uses its internal pressure sensor to maintain altitude. If the aircraft starts to descend, the internal pressure sensor will detect an increase in pressure and signals the InstantEye to increase thrust. This creates an artificial pressure increase beneath the rotors lifting the aircraft back to the desired altitude. This was a common occurrence during our experiment, and usually resulted in overshooting the desired altitude, oscillating up and down until equilibrium was reached. This phenomenon was exacerbated by wind gusts, turbulence, and operating near the ground in the presence of ground effect, but a time-running average helped mitigate this in our temperature analysis. Since our sample size is small, we would expect to see altitude oscillations appear in the results. Large oscillations would translate into more variation in the pressure measurements and produce a less accurate mean. Observing data points of Figure 25 suggests that while the InstantEye was in flight very few altitude oscillations were occurring since the variation is similar for both cases. This is not the case if Figure 24, suggesting altitude oscillations were significant.
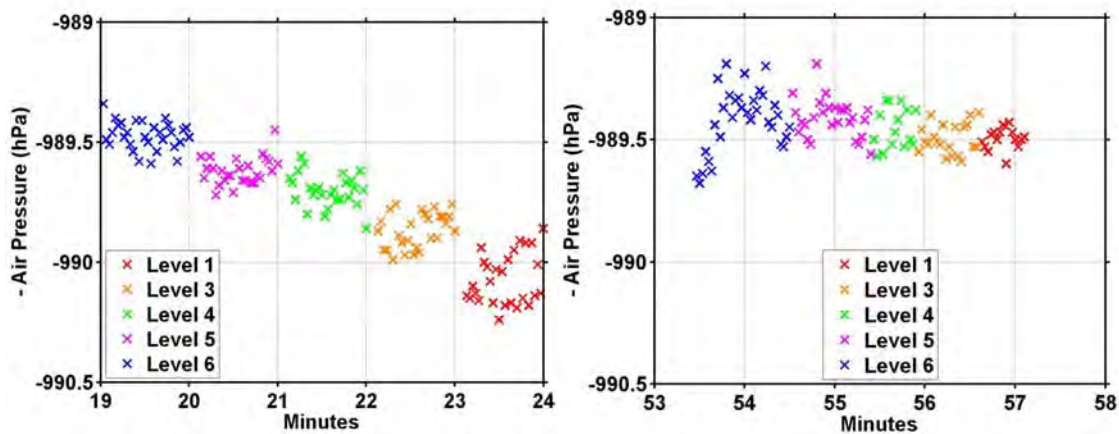

Figure 25.   InstantEye pressure effect from Guest's experiment (shown negative as a proxy for elevation), left–InstantEye in flight, right–held by hand props off (courtesy of Dr. Peter Guest)

Our results do present an interesting finding: the mean pressure increase by the radiosonde in flight was at least 0.12 hPa above the mean pressure when

held by hand at each level. Data in Figure 25 at level six appear to confirm this pressure bias when in flight. This means while hovering at any altitude we can expect to observe a 0.12 hPa pressure measurement bias, translating into a 1 m altitude bias. Guest's observations suggest that pressure will further increase below 1.3 m as the surface is approached due to ground-effect. While we did not observe this to be true in our observations, large altitude oscillations may explain this inconsistency.

THIS PAGE INTENTIONALLY LEFT BLANK

VI. CONCLUSIONS

A. SUMMARY OF EXPERIMENT

This experiment is one of the first studies to analyze quad-rotor effects on meteorological sensors. Our use of an RS92 radiosonde onboard the InstantEye sUAS produced some important results. In unstable temperature profiles, temperature measurements made in the surface layer are as accurate as the manufacturers claimed accuracy for surface measurements. In stable temperature profiles mixing occurs below 1.3 m, smoothing out the temperature gradient making it difficult to differentiate between levels. Above 2 m in stable conditions, temperature measurements were warmer than expected; suggesting air is originating from as high as 2 m aloft. The InstantEye's rotors contribute to the variation in temperature measurements, and this effect is strongest near the surface. The variations introduced by the prop-wash help suppress variations by turbulent fluctuations, but are present above the surface layer. The InstantEye also introduces a 0.12 hPa pressure bias while in flight due to the pressure effects of the rotors corresponding to a 1 m elevation bias. While we could not quantify the presence of ground-effect in our results, other experiments have shown ground-effect to introduce a pressure bias of 0.60 hPa (5 m altitude error) near the surface.

B. OPERATIONAL APPLICABILITY

This experiment must also be considered in the correct context. Our flights were conducted in extreme meteorological conditions, since we were confined to the surface layer in a desert-like environment. The atmosphere was dry, and strong temperature gradients dominated lower levels during unstable flights. As a result, turbulent fluctuations were intense during unstable temperature conditions. In a real naval application, our InstantEye-radiosonde combination would be used at sea, where there is obviously a surface humidity source, and temperature gradients are generally not as strong. As a result turbulent

fluctuations of temperature would be less prominent, but humidity fluctuations would be stronger.

Our experiment also required hovering the InstantEye for periods of time in one location. This was to obtain sufficient data for statistical analysis since our reference tower was limited to the lowest five meters. Taking multiple measurements while hovering helps reduce uncertainty and improve accuracy, but it is suspected that hovering also gives time for rotor contamination to take hold mixing the ambient air. In practice, the aircraft and sensor would ascend to an altitude of about 600 to 900 meters to sample a large vertical profile in the boundary layer. Constantly moving upward is advantageous for meteorological sensing because it also reduces the induced velocity through the rotors, as we saw in Chapter II.

C.   RECOMMENDATIONS FOR FUTURE RESEARCH

There were several limitations to our experiment that warrant further investigation. Trials above the surface layer are a logical next step forward to investigate the effects of prop-wash on vertical motion, both upward and downward, and measurement uncertainty in the absence of strong turbulent fluctuations. Our results suggest that measurements taken in an unstable atmosphere will perform very well above the surface layer, but it is unclear if rotor mixing will significantly bias temperature and humidity accuracy in stable atmospheres, or if there is a dependency on the strength of the gradient.

Sea trials are necessary to observe the effects of prop-wash on humidity since we did not have a strong humidity gradient in our experiment. Flights originating from ships would also reveal operating considerations and limitations for future use in a naval weather-sensing program. Furthermore, other meteorological sensors could be used in place of Vaisala's RS92, as well as an alternative to the InstantEye. There are numerous combinations of quad-rotors and sensors that could be used in place of our equipment to optimize sensor placement and accuracy, as well as identify an ideal cost-benefit relationship.

74

LIST OF REFERENCES

Braun, S. A., R. Kakar, E. Zipser, G. Heymsfield, C. Albers, S. Brown, J. Zawislak, 2013: NASA's genesis and rapid intensification processes (GRIP) field experiment. *Bulletin of the Amer. Meteor. Society*, **94**, 345–363.

Cady-Pereira, K. E., M. W. Shephard, D. D. Turner, E. J. Mlawer, S. A. Clough, and T. J. Wagner, 2008: Improved daytime column-integrated precipitable water vapor from Vaisala radiosonde humidity sensors. *J. Atmos. Ocean Tech.*, **25**, 873–883.

Campbell Scientific, cited 2015: "CR3000 Micrologger users manual." [Available online at: https://s.campbellsci.com/documents/us/manuals/cr3000.pdf.]

Campbell Scientific, cited 2015: "FW05, FW1, and FW3 thermocouple brochure." [Available online at https://s.campbellsci.com/documents/us/product-brochures/b_fw05-fw3.pdf.]

Kruis, F. E., H. Fissan, and A. Peled, 1998: Synthesis of nanoparticles in the gas phase for electronic, optical and magnetic applications—A review. J*. Aerosol Sci.*, **29**, 511–535.

Fairall, C. W., E. F. Bradley, D. P. Rogers, J. B. Edson, and G. S. Young, 1996: Bulk parameterization of air-sea fluxes for tropical ocean-global atmosphere coupled-ocean atmosphere response experiment. *J. Geophys. Res.,* **101,** 3747– 3767.

Garratt, J. R., 1992: *The Atmospheric Boundary Layer*. Cambridge University Press, 316 pp.

Gallaudet, T. C., 2014: "Naval Meteorology and Oceanography Command priorities for 2014–2115," NAVMETOCCOMNOTE 3120, DON.

Guest, S., and C. Machado, 2015: "Using UAS to sense the physical environment and predict electromagnetic system performance," NPS Research Program, prepared for OPNAV N2/N6E, NPS-MR-15–001.

Jauhiainen, H., P. Survo, R. Lehtinen, J. Lentonen, 2014: "Radiosonde RS41 and RS92 key differences and comparison test results in different locations and climates," WMO TECO on Meteor. and Env. Instruments [Available online at: https://www.wmo.int/pages/prog/www/IMOP/publications/IOM-116_TECO-2014/Session%203/P3_16_Juhiainen_Radiosonde_RS41_RS92_Key_Differences_Comparison_TestResults.pdf.]

Keane, J., and S. Carr, 2013: A brief history of early unmanned aircraft, *Johns Hopkins APL Technical Digest*, **32**, 3, 558–571.

Ko, H., J. Sari, and J. Skura, 1983: Anomalous microwave propagation through atmospheric ducts, *Johns Hopkins APL Technical Digest*, **4**, 1, 12–26.

Layton, D., 1984: *Helicopter Performance*, Matrix Publishers, 198 pp.

Leishman, G. J., 2006: *Principles of Helicopter Aerodynamics*, (2nd ed.), Cambridge University Press, 814 pp.

Moti, M., cited 2015: "Vaisala RS41 trial in the Czech Republic," Vaisala News 192/2014, [Available online at: http://www.vaisala.com/Vaisala%20Documents/Vaisala%20News%20Articles/VN192/VaisalaNews192_Czech%20Trials.pdf.]

NRL, 2015: "Trident warrior 2013," NRL Technical memorandum v1.5

OPNAV N2/N6, 2012: "Navy strategy for achieving information dominance: optimizing Navy's primacy in the maritime and information domains," DON,

OPNAV N2/N6F5, 2010: Termination of the upper air sensing/mini-rawinsonde system (MRS) AN/UMQ-12A program, memo #3140, s/n N2N6F5/0U152815.

Pentagon, cited 2015: "Unmanned systems integrated roadmap FY2013–2038," Reference Number: 14-S-0553, [Available at http://www.defense.gov/pubs/DOD-USRM-2013.pdf.]

Petty, G., 2008: *A first Course in Atmospheric Thermodynamics*, Sundog Publishing, 338 pp.

Physical Sciences Inc., 2012: *InstantEye User Manual*.

Reineman, B., L. Lenain, N. Statom, and K. Melville, 2013: Development and testing instrumentation for UAV-based flux measurements within terrestrial and marine atmospheric boundary layers, *J. Atmos. Ocean. Tech.*, **30**, 1295–1319.

Rotronic Corp., cited 2015: "MP100H data sheet," [Available online at http://www.rotronic.com.sg/_upload/gen_downloads/DatasheetMP100A.pdf.]

Stull, R. B., 1988: *An Introduction to Boundary Layer Meteorology*, Kluwer Academic Publishers, 667 pp.

Tayebi, A., and S. McGilvray, 2006: Attitude stabilization of a VTOL quadrotor aircraft, *IEEE Transactions on Control Systems Tech.*, **14**, 3, 562–571.

Taylor, J. R., 1997: *An Introduction to Error Analysis: The Study of Uncertainties in Physical Measurements,* (2nd ed.), University Science Books, 283 pp.

Taylor, W. R., 1977: *Jane's Pocket Book of Remotely Piloted Vehicles*, Collier Books.

U.S. Joint Chiefs of Staff (JCS), 2010: Joint Publication 3–52, Joint Airspace Control Washington, D.C.

Vaisala Corp., cited 2014: "Vaisala weather transmitter WXT520 data sheet," [Available online at http://www.vaisala.com/Vaisala%20Documents/Brochures%20and%20Datasheets/WEA-MET-WXT520-Weather-datasheet-B210417EN-K-LOW.pdf.]

Vaisala Corp., cited 2013: "Vaisala radiosonde RS92-SGP data sheet," [Available online at http://www.vaisala.com/Vaisala%20Documents/Brochures%20and%20Datasheets/RS92SGP-Datasheet-B210358EN-F-LOW.pdf.]

Vaisala Corp., cited 2010: "Revised solar radiation correction table RSN2010 for RS92 temperature sensor," Vaisala, Sounding Data Continuity tables, [Available online at: http://www.vaisala.com/en/meteorology/products/soundingsystemsandradiosondes/soundingdatacontinuity/RS92-Data-Continuity/Pages/revisedsolarradiationcorrectiontableRSN2010.aspx.]

Vömel, H., and Coauthors, 2007: Radiation dry bias of the Vaisala RS92 humidity sesnor, *J. Atmos. Ocean. Tech.*, **24**, 953–963.

Yoneyama, K., M. Fujita, N. Sato, M. Fujiwara, Y. Inai, and F. Hasebe, 2008: Correction for radiation dry bias found in RS 92 radiosonde data during the MISO field experiment. SOLA, **4**, 013–016.

THIS PAGE INTENTIONALLY LEFT BLANK

INITIAL DISTRIBUTION LIST

1. Defense Technical Information Center
   Ft. Belvoir, Virginia

2. Dudley Knox Library
   Naval Postgraduate School
   Monterey, California